Thesis for a Ph.D. Degree

동아시아 온대저기압과 이들의 미래 온난 기후에서의 변화

February 2023

School of Earth and Environmental Sciences
Graduate School
Seoul National University

Jaeyeon Lee

East Asian extratropical cyclones and their possible changes in a warming climate

By

Jaeyeon Lee

A Dissertation Submitted to the Faculty of the Graduate School of the Seoul National University in Partial Fulfillment of the Requirement for the Degree of Doctor of Philosophy

Degree Awarded:

February 2023

Advisory committee:

Professor	Chang Hoi Ho, Chair
Professor	Seok-Woo Son, Advisor
Professor	Jung-Hoon Kim
Professor	Baek-Min Kim
Professor	Soon-Il An

이학박사학위논문

동아시아 온대저기압과 이들의 미래 온난 기후에서의 변화

East Asian extratropical cyclones and their possible changes in a warming climate

2023년 2월

서울대학교 대학원

지구환경과학부

이 재 연

East Asian extratropical cyclones and their possible changes in a warming climate

동아시아 온대저기압과 이들의 미래 온난 기후에서의 변화

지도교수 손 석 우

이 논문을 이학박사 학위논문으로 제출함

2022년 10월

서울대학교 대학원

지구환경과학부

이 재 연

이재연의 이학박사 학위논문을 인준함

2023년 1월

위 원 장_____(인)

부위원장_____(인)

위 원_____(인)

위 원_____(인)

위 원_____(인)

Abstract

Extratropical cyclones (ETCs) are one of the essential mid-latitude systems accompanied by various weather phenomena over East Asia, e.g., heavy rainfall and yellow dust event; thus, it is essential to understand their climatic features and explore how they will be changed in a warming climate. In this study, ETCs are detected and tracked on the 850-hPa relative vorticitiy field using a Lagrangian tracking algorithm which can provide insight into the detailed characteristics of individual ETCs.

In observation (ERA-Interim reanalysis data), East Asian ETCs are primarily generated in the downstream regions of the Altai-Sayan Mountains and the Tibetan Plateau and over the Kuroshio-Oyashio Extension. They are most active in Mongolia and Kuroshio Current region and intensify rapidly over the Kuroshio-Oyashio Extension, where the sea surface temperature gradient is sharp. Among them, the continental ETCs, e.g., Mongolia and East China ETCs generated from downstream regions of the Altai-Sayan Mountains and the Tibetan Plateau, are most frequent in spring rather than in winter when baroclinicity is the strongest. In addition, these continental ETCs have significant decreasing trends in spring and summer.

These climatic features in observation are well captured in the

historical simulations of CMIP5 models. Only nine CMIP5 models with no missing values over high-terrain regions are selected in this study since the missing values could lead to difficulty in tracking the incipient ETCs near mountains. Nevertheless, there are still noticeable biases in and downstream of the high-terrain regions. Such biases are particularly pronounced in the models with a coarse spatial resolution and a smooth topography which weakens lee cyclogenesis. The best five models, which show better performance for historical simulations than other models, are used to evaluate the possible changes of East Asian ETCs under the RCP8.5 scenario. East Asian ETCs are projected to decrease and weaken in a warming climate, resulting in decrease of ETC-related precipitation near Korean peninsula and Japan. This response of East Asian ETCs to increasing greenhouse gas forcing is also shown in the latest climate models (CMIP6). These ETC property changes are largely consistent with decreased baroclinicity in the upstream region of the location where the strongest weakening of ETCs is projected; the change of baroclinicity is contributed by enhanced static stability and reduced vertical wind shear in a warming climate.

The relationship between weakened ETCs and decreased baroclinicity in a warming climate is confirmed in the idealized experiments manipulating background jet amplitude and potential

temperature profile. In these experiments, the ETC strengths weaken under weakened baroclinic conditions, supporting the result of CMIP study that the weakening of local baroclinicity could play a critical role in determining the future changes of East Asian ETCs. The experiments also provide the possibility that ETC strengths could non-monotonically respond to background baroclinicity change under the baroclinically highly unstable condition. It implies that ETCs cannot be explained by only baroclinicity under strongly increasing baroclinicity.

Key Words: Extratropical cyclones, East Asia, Automated tracking algorithm, Global warming, CMIP5, Idealized experiment

Student Number: 2018-37296

Table of Contents

List of Figures

List of Tables

Chapter 1. Introduction

1.1 Climatic features of East Asian ETCs

Extratropical cyclones (ETCs) are weather system transporting energy the subtropics to higher latitudes and accompany with various weather events in the mid-latitude. They often have major socio-economic impact occurring extreme precipitation with strong winds (Lamb and Frydendahl 1991; Fink et al. 2009; Della-Marta and Pinto 2009). The ETCs are also an important component of the mid-latitude water cycle. The ETCs contribute to 80–90% of the total precipitation climatology (Hawcroft et al. 2012). Due to this importance of ETCs, there have been many efforts to understand climatic features of ETCs in East Asia.

Climatic features of extratropical cyclones (ETCs) in East Asia have been widely documented in the literature after the pioneering work by Chung et al. (1976). By manually detecting and tracking ETCs in the year1958, Chung et al. (1976) reported that East Asian ETCs typically develop on the leeward side of major mountain barriers, similar to the development of lee cyclones in the Canadian Rockies. Whittaker and Horn (1984) confirmed this finding by extending the analysis to a more extended period (1958–1977). They found that East Asian ETCs

commonly form along the east coast of South China. These oceanic (or coastal) ETCs are generally stronger than continental ETCs. Chen et al. (1991) later updated the work of Whittaker and Horn (1984) by examining daily surface weather maps for the period 1958–1987. The leeward cyclogenesis region downstream of the Altai–Sayan Mountains and the coastal cyclogenesis region over warm ocean water from the East China Sea to the East Sea/Sea of Japan were identified as the main regions of cyclogenesis in their study (see Fig. 1.1a for the geographical locations of these regions and sea surface temperature (SST)).

The above studies manually detected and tracked ETCs with12-hourly or daily surface weather maps. This approach could be acceptable for studying extreme or well-defined ETCs but might have difficulty in examining weak and relatively small-scale ETCs. To overcome this caveat and to utilize gridded dataset, recent studies have used automated algorithm (see the review by Neu et al. (2013)). It allows for detecting and tracking a large number of ETCs systematically and objectively. The automated algorithm is particularly advantageous for long-term gridded datasets.

A series of studies have utilized an automated algorithm to study East Asian ETCs. Adachi and Kimura (2007) constructed the cyclogenesis and ETC track density maps in East Asia by applying the nearest-

neighbor method to 6-hourly surface pressure field obtained from a reanalysis data. They reaffirmed the previous findings that active cyclogenesis regions are distributed along the leeward side of mountains and the Kuroshio Current and the Kuroshio-Oyashio Extension (hereafter simply Kuroshio region). By separately examining the merging and splitting of ETCs, Inatsu (2009) found that ETC merging is frequent in the western North Pacific. He reported that the merged ETCs develop more rapidly than other ETCs. Zhang et al. (2012) used the mean sea level pressure (MSLP) field to detect and track ETCs and found that the West Siberian plain, Mongolia, and the coastal regions of South China are major cyclogenesis regions. Chen et al. (2014), who applied a Hodges' algorithm (Hodges et al. 1999) to 6-hourly relative vorticity field, further reported that Mongolia (including the Altai–Sayan Mountains) is a primary source region for East Asian ETCs while South China is a secondary source region.

The factors that determine ETC developments, especially for rapidly developing ETCs which are often referred to as explosive cyclones or meteorological bombs (Sanders and Gyakum 1980), have also been examined. Unlike normal ETCs, explosive ETCs are mainly observed over the East Sea/Sea of Japan and the northwest Pacific near the Kuroshio Current (e.g., Chen et al. 1992). This bimodal distribution in space, which

has a local minimum over the islands of Japan, is explained by intense heat transport from warm ocean currents around Japan (e.g., Chen et al. 1992; Yamamoto and Hirose 2007) and enhanced low-level baroclinicity due to a sharp SST gradient (e.g., Yoshida and Asuma 2004), indicating that development of East Asian ETCs is quite sensitive to SST.

Most of the aforementioned studies, however, are focused on cyclogenesis and cyclone frequency. Other properties, such as ETC intensity, lysis, developing rate, lifetime and traveling speed, are not well documented. More importantly, most studies are primarily focused on cold-season ETCs. As such, the seasonal cycle of East Asian ETCs is not fully understood. Adachi and Kimura (2007), for instance, showed that ETCs that develop from the mouth of the Yangtze River and the East China Sea to the northeastern region of Taiwan have the maximum cyclogenesis in winter. However, Wang et al. (2009) documented that ETCs in Mongolia and northeastern China have a maximum frequency in spring. It is also unclear whether East Asian ETCs have undergone any long-term changes. Wang et al. (2009) reported that the ETC frequency and intensity were significantly decreased in the 40°–45°N latitude band during the last few decades. Chen et al. (2014) and Cho et al. (2018) also documented a weakening of wintertime ETCs in China and a decreasing number of springtime ETCs in southern China, respectively. In contrast,

Iwao et al. (2012) showed that the number of explosive cyclones has slightly increased in the east of Japan. These studies, however, are based either on a relatively small domain (e. g. Mongolia and northeastern China) or just for one season. A comprehensive analysis covering all of East Asia (Fig. 2.1a) and for all four seasons has not been conducted with the modern reanalysis data.

The present study aims to extend and update previous studies by documenting more detailed statistics of East Asian ETCs. Analyses are not limited to cyclogenesis and cyclone frequency but conducted for various other ETC properties. Their seasonal cycle and long-term trends are also quantitatively evaluated. Unlike the previous studies that utilized the MSLP field, the present study identifies ETCs on the 850-hPa relative vorticity field (Hoskins and Hodges 2002). The MSLP field was traditionally used for ETC detection and tracking. Either the local minimum or its gradient is particularly used to define the center of ETC. Although this approach is successful in capturing a well-organized cyclone, it often misses weak and unorganized cyclones particularly over the complex terrain (Sinclair 1994; Hodges 1999) as in East Asia (Fig. 2.1a). In this regard, the relative vorticity is advantageous because it allows for the early detection of weak and less-organized ETCs (Hoskins and Hodges 2002). The 850-hPa isobaric surface is also practically useful

as it minimizes the negative effects of underground extrapolation except over the Tibetan Plateau (Chen et al. 2014).

The ETC development, especially for abruptly deepening ETCs which are referred as to as explosive cyclones (Sanders and Gyakum 1980), have received an attention due to their severe weather impact (Wernli et al. 2002). The previous studies on these explosive cyclones have helped unveil various dynamic and physical processes which are responsible for intensification of ETCs.

The explosive ETCs mainly occur over East Sea and the northwest Pacific near Kuroshio Current (Sanders and Gyakum 1980; Chen et al. 1992). These regions are adjacent to warm ocean current which is a favorable condition for supplying warm and moist air to ETCs. The supplied moisture ascends along the warm conveyor belt in ETC and condenses with latent heat release (Madonna et al. 2014). These diabatic heating processes are maximized in middle troposphere and plays a major role for intensification of ETCs. The maximum diabatic heating in the mid-troposphere induces the positive potential vorticity (PV) anomaly below. The positive PV anomaly in the lower troposphere strengthens the cyclonic rotation.

East Asia is also the region where the upper-level wave activities (e. g., enhanced upper-level trough and Rossby wave breaking) are frequent

(Chang et al. 2002). The upper-level wave activities shown as the positive PV anomaly in the upper troposphere exert the cyclonic rotation in the middle to lower troposphere (Hoskins et al. 1985). The previous studies confirmed that the development processes of East Asian ETCs are associated with both the diabatic processes on the lower troposphere and the upper-level wave activities on the upper troposphere in case studies (Lee et al. 1991; Lee et al. 2009; Heo et al. 2015; Heo et al. 2019).

In this study, development processes of East Asian ETCs are investigated in perspectives of baroclinic instability and PV dynamics. In addition, their development processes are going to be used to understand their surface weather impact on East Asia, since ETC intensity and background moisture during their intensification are closely associated with precipitation accompanied by ETCs (Pfahl and Sprenger 2016).

1.2 The possible response of East Asian ETCs to climate change

The advent of an automated algorithm has allowed to simulate ETC properties using general circulation model (GCM) produced dataset. The GCM studies on ETCs are helpful to understand the possible response of ETC properties to climate change (e. g., the response of ETCs to increasing

greenhouse gas concentration). The early GCM studies on ETCs have tried to compare and validate the simulated ETC properties with the features of ETCs in reanalysis data.

The spatiotemporal distributions of ETCs are well represented in GCMs. The GCMs successfully reproduce storm tracks over the North Pacific, the North Atlantic, and the Mediterranean and their seasonality (Riable et al. 2010; Eichler et al. 2013; Pinto et al. 2016; Yang et al. 2018). Riable et al. (2007) applied the automated algorithm to the output from a low-resolution (T31 resolution) climate model and reported that the simulated ETC frequency is similar to the observed patterns, but it is underestimated mainly in the Mediterranean region. Bengtsson et al. (2006) confirmed that the cyclogenesis regions resemble to the reanalysis data (ERA-40) using the ECHAM5 (T63 resolution) models. They are also pointed to the underestimated cyclogenesis in the leeward side of the Rocky Mountain and suggested that these deficits come from lower model resolution and coarser orography in GCMs than in reanalysis data. Although a coarse spatial resolution with a smooth topography often causes the GCMs to underestimate ETC frequency and intensity (Blender and Schubert 2000; Bengtsson et al. 2009; Colle et al. 2013; Seiler and Zwiers 2016; Seiler et al. 2018), a reasonable model performance allows the use of GCMs for examining future changes of

ETCs at least in quality.

A majority of modeling studies have reported that the number of ETCs in the NH mid-latitudes may decrease in a warming climate, while their mean intensity does not change much. A reduced ETC frequency has been attributed to the weakened baroclinicity due to the accelerated high-latitude warming in response to increasing greenhouse gas concentrations (Bengtsson et al. 2006; Chang et al. 2012; Lambert and Fyfe 2006; Pinto et al. 2007). Such changes in baroclinicity are likely adverse to those in diabatic processes. It has been suggested that increased moisture content in a warming climate could enhance the latent heat release within ETCs which can strengthen ETCs (Stoelinga 1996; Ahmadi-Givi et al. 2004; Seiler 2019). Their relative importance, however, remains to be determined.

Although there exists a consensus on the projected ETC changes at the hemispheric scale, they differ at regional scales. For instance, Bengtsson et al. (2006) suggested a reduced ETC frequency near the Mediterranean but an increased ETC frequency near the British Isles in the late 21st century. Pinto et al. (2007) reported a reduced number of ETCs at the Pacific North Coast of Canada and north of Scandinavia in a warming climate but essentially no change at the Eastern North Atlantic. By examining the best seven CMIP5 models which reproduce realistic

ETC properties over the eastern United States and western Atlantic, Colle et al. (2013) concluded that ETC density would decrease over the western Atlantic but increase over the eastern United States in a warming climate. Zappa et al. (2013) reported that the wintertime ETCs tend to decrease, but intense ETCs would increase over the North Atlantic and Europe under the climate change scenarios.

These studies suggest that the future projection of ETCs is dependent on geographical regions. However, unlike in North America and Europe, the projected ETC changes in East Asia have not been well documented. Model biases are also not well reported over East Asia, although the complex topography in the region, such as the Tibetan Plateau and the Altai-Sayan Mountains northeast of the Plateau, can introduce significant biases in lee cyclogenesis. Since East Asian ETCs traverse densely populated regions and cause significant socioeconomic impacts (Lee et al. 2016; Kim et al. 2021), their properties in climate models and their future changes need to be better understood.

The present study aims to quantify the biases of the Coupled Model Intercomparison Project phase 5 (CMIP5) models in the context of genesis, frequency, and intensity of East Asian ETCs, and to evaluate the future changes of East Asian ETCs. Because the CMIP5 models are utilized in this study as they have not been examined in the study of East Asian

ETCs, the analysis of future changes of East Asian ETCs will be examined using CMIP5 models first. After that, the key findings of the CMIP5 study is used as references for the CMIP6 model evaluations. Beyond this, as ETC is one of the important midlatitude systems that determine local precipitation, possible changes of precipitation associated with East Asian ETCs in a warming climate is also investigated using the CMIP6 models.

1.3 Extratropical cyclones in idealized simulations

Differential solar heating from the tropics to the poles can lead to a temperature gradient, inducing that small perturbation grows into matured ETC through baroclinic instability (Charney 1947; Eady 1949). IPCC (2004) reported that global temperature is expected to increase but also strong polar warming to enhance in last. Baroclinicity associated with temperature gradient can provide favorable conditions for the evolution of ETC and cyclogenesis. Thus, there have been many efforts to understand how global warming changes baroclinicity in Northern Hemisphere.

Future change in temperature leads to horizontal and vertical temperature gradients related to wind shear and static stability. As confirmed by observations, polar amplification lowers the lower

troposphere's meridional temperature gradient–a typical winter trend (Wang et al. 2017). Furthermore, the observed upper tropospheric warming at the tropics and lower stratospheric cooling at high latitudes can raise the meridional temperature gradient near tropopause at midlatitudes and change the vertical temperature gradient (Collins et al. 2013). Since these future changes in upper and lower baroclinicity are compensating with each other, it is not easy to fully understand their net effect on ETCs.

The increase of temperature in a warming climate is expected to increase atmospheric moisture content (Held and Soden 2006), leading to enhanced latent heating within ETC. Furthermore, the strengthened latent heating in a warming climate could enhance ETC strength (Marciano et al. 2015). For this reason, idealized modeling has been used to examine ETC's response to increased moisture content. Booth et al. (2013) performed two idealized experiments: one by applying different initial relative humidity and the other by varying saturation vapor pressure with the same initial relative humidity. As a result, they showed that ETC intensity–defined as sea level pressure and vertically integrated eddy kinetic energy–can be strengthened with increased moisture content, reconfirmed by Pfahl et al. (2015), who performed an idealized model with different moisture content adjusted by manipulating optical

thickness.

Such enhanced latent heating could directly strengthen ETC but indirectly weaken it. The latent heating is likely to increase the static stability and weaken baroclinicity, inhibiting the development of ETC (O'Gorman 2011). Due to this complex interaction between future changes in latent heating and baroclinicity, their net effect on ETC has been investigated using idealized modeling. Tierney et al. (2018), who performed idealized experiments that modified upper level zonal wind, leading to change in baroclinicity, and bulk static stability, resulting in a change in atmospheric moisture content, found that ETC strength is more dependent on initial background states than moisture content. ETC strength responses to changes in baroclinicity and moisture content are not monotonic. Rantanen et al. (2019) and Kirshbaum et al. (2018) exhibit that the response of ETC strength to increasing moisture content depends on initial temperature. Furthermore, Rantanen et al. (2019) stated that surface cyclones were affected by upper level baroclinicity only in moist simulation, indicating the improvement of the interaction of upper and lower level baroclinicity by the diabatic process.

There have been many previous studies to understand the response of ETCs to change in baroclinicity and the role of moisture content. However, most previous studies tried to understand ETC's response to

baroclinicity changes by solely manipulating the initial horizontal temperature gradient. Our CMIP5 results found the horizontal temperature gradient change, represented by wind shear, and the vertical temperature gradient, represented by static stability, in the East Asian region where the weakening of ETCs exists. Therefore, in this study, we will conduct an idealized experiment by changing both the initial horizontal temperature gradient and the initial vertical temperature gradient; to try to understand the relationship between the change in the background states and ETCs in East Asia with increased moisture content.

1.4 Aims of the thesis and outline

The previous studies have tried to understand the general characteristics, variations, and the response of ETCs to the anthropogenic forcing. However, there are still some questions on ETCs.

The studies on ETC climatology on a hemispherical scale typically focused on the oceanic ETCs which have stronger signal than the continental ETCs, even the regional studies are mostly conducted about ETCs over North America or Europe. There are a few studies on East Asian ETCs like Adachi and Kimura (2007) but they did simple analysis on ETC properties (e. g., tracks and genesis locations). There are also some previous studies on East Asian ETC development, but they are

based on case studies. So, it needs to understand the general development processes of East Asian ETCs using long-term data.

Since the previous studies on ETCs in a warming climate mentioned the needs for regional studies, there have been the effort to understand the response of ETCs to the anthropogenic forcing on a regional scale in North America and Europe. However, the projected change of East Asian ETCs under global warming scenario are not fully understood. Therefore, possible future changes in ETCs and their possible mechanism need to be examined. Future change in East Asian ETCs will be investigated using CMIP5 and 6 models; possible mechanism of the response of East Asian ETCs to atmospheric CO2 concentration will be understood by an idealized experiment in this paper.

The main purposes of this study are 1) to revisit East Asian ETC climatology, 2) to identify the general development processes of East Asian ETCs with their surface weather impacts, 3) to explore change in background state and ETCs in East Asia in different climate regimes (warming and cooling climates) in GCMs, and 4) to explore causality of changes in East Asian background state and East Asian ETCs in an idealized modeling.

The rest of this paper is organized as follows. The detailed climatic features and seasonal variations of East Asian ETCs are investigated in

Section 2. The development processes of continental East Asian ETCs, which can affect East Asian weather, are also identified in Section 2. The ETC simulations of GCMs and the changes of East Asian ETCs and their related precipitation in a warming climate scenario are evaluated and explored in Section 3. The relationship between changes in ETCs and background states in East Asia is explored using an idealized experiment in Section 4. The contents in Section 2 are from Lee et al. (2016) and Lee et al. (2020), and the contents in Section 3 are from Lee et al. (2022).

Chapter 2. Data and Methods

2.1 Data

In reanalysis study on East Asian ETCs, we used 6-hourly output of the European Centre for Medium-Range Weather Forecasts (ECMWF) Re-Analysis Interim (ERA-Interim) (Dee et al. 2011) for the period of 1979–2018 for examining climatic features, seasonality, and long-term trends.

In climate models study, among CMIP5 and 6 models (Taylor et al. 2012; Eyring et al. 2016), we used nine CMIP5 models and six CMIP6 models which provide 6-hourly output and have no missing values in high terrain region, because missing values over mountains make lee cyclone detection difficult. All models used in this study are listed in Table 2.1 and 2.2. All datasets are interpolated to a 1.5°x1.5° spatial resolution. We first compare the CMIP5 and 6 historical runs for the period of 1979–2004 with the ERA-Interim. The future changes of East Asian ETCs are then quantified by subtracting the CMIP5 and 6 historical runs from the Representative Concentration Pathway 8.5 (RCP 8.5) and the Shared Socioeconomic Pathway 5 8.5(SSP5-8.5) runs for the period of 2074–2099. The annual ETC statistics from a single ensemble member are primarily examined in this study.

Table 2.1. List of the CMIP5 models used in this study. The Best5 models are indicated with asterisk. The terrain change is quantified by spatial standard deviation of terrain height over the domain shown in Fig. 4.1a.

Label	Model Name	Atmosphere Model Resolution (°lat x°lon)	Terrain Change (m) (ERA-Interim: 1499.89)
1	BCC-CSM1-1-m	1.1x1.1	1427.54
2	BNU-ESM	2.8x2.8	1437.07
3	*CanESM2	2.8x2.8	1440.07
4	*CMCC-CM	0.7x0.7	1527.81
5	*CNRM-CM5	1.4x1.4	1495.93
6	INM-CM4	2.0x1.5	1394.90
7	*MPI-ESM-MR	1.9x1.9	1474.18
8	*MPI-ESM-LR	1.9x1.9	1474.18
9	NorESM1-M	2.5x1.9	1371.64

Table 2.2. List of the CMIP6 models used in this study.

Label	Model Name	Atmosphere Model Resolution (°lat x°lon)
1	BCC-CSM2-MR	0.56x1.125
2	MPI-ESM1-2-HR	1.25x0.9
3	MPI-ESM1-2-LR	2.5x1.8
4	EC-Earth3	0.94x0.7
5	NorESM2-MM	1.25x1.25
6	NorESM2-LM	2.5x2.5

2.2 ETC detection and tracking

In reanalysis study, ETCs are automatically detected and tracked by applying the algorithm, which was originally developed by Hodges (1994, 1995, 1999), to the 6-hourly relative vorticity field from ERA-Interim dataset. This algorithm has been evaluated well and applied to various datasets, such as reanalysis data (e.g., Hoskins and Hodges 2002), general circulation model output (e.g., Bengtsson et al. 2006), and regional climate model output (e.g., Côté et al. 2015) for both global and regional ETC studies (Grise et al. 2013; Zappa et al. 2013; Chen et al. 2014; Plante et al. 2015).

To define synoptic scale ETCs, the relative vorticity field is first filtered at a T42 spectral resolution, which contains the total wavenumbers within a range from 5 to 42. This filtering effectively removes the background flow and small-scale disturbances. A segmentation technique, called "connected component labeling", is then applied to identify the local maximum of relative vorticity. The local maximum is defined at three consecutive time steps (at six-hour increment), and the smoothed trajectory is calculated by considering the direction and speed of the moving ETC (Hodges 1994, 1995, 1999).

In this study, quasi-stationary thermal lows, which do not intensify with time, are removed by considering ETCs only with a minimum

intensity greater than 1.0 x 10-5 s^{-1} (or 1 cyclonic vorticity unit; CVU), a lifetime longer than two days, and a traveling distance greater than 1000 km (Hoskins and Hodges 2002; Grise et al. 2013). Tropical cyclones and their transitions into ETCs are excluded by neglecting all detected cyclones that travel across 25°N from the tropics.

In climate model study, ETCs in both reanalysis and model datasets are objectively detected and tracked by using an automated tracking algorithm (Hodges 1994, 1995, 1999). Since the extrapolation errors over the high terrain region can be partly alleviated when using the isobaric surface in the lower troposphere (Chen et al. 2014), the 850-hPa relative vorticity field is used in ETC detection and tracking, as has been used by Hoskins and Hodges (2002) and Lee et al. (2020). To focus on synoptic-scale ETCs, the planetary-scale background flow and small-scale perturbations are filtered out by truncating the relative vorticity field into T42 resolution.

The ETC center, defined as a local maximum of 850-hPa relative vorticity, is tracked. The resultant track is smoothed by minimizing a cost function of travel distance and direction. Only ETCs initiated north of 25°N and stronger than 1.0 x 10-5 s^{-1} (or 1 cyclonic vorticity unit; CVU) are considered to exclude tropical cyclones and un-organized cyclones. Further details can be found in Hoskins and Hodges (2002) and Lee et al.

(2020).

2.3 ETC statistics

The ETC statistics are computed for frequency, intensity, genesis and lysis locations, growth rate, decay rate, lifetime, speed, and traveling distance. A definition of each property is explained in Table 2.3. In all cases, ETC statistics are shown in latitude-longitude grids with a 1.5° grid spacing. The statistics at a given grid point represent ETCs within an effective radius of 555 km (e.g., Grise et al. 2013). For instance, one ETC at a given grid point implies that the grid point is influenced by at least one ETC, which is located within a 555-km radius. As such, the same ETC can be counted at multiple grid points. If the same ETC is counted more than once at a given grid point (this is the case when the ETC is moving slowly), only the first occurrence is considered.

Table 2.3. Definition of ETC properties.

ETC Property (unit)	Description
Cyclogenesis (# month^{-1})	The initial point of the detected cyclones (or the first location where ETC intensity becomes stronger than 1 CVU).

Frequency (# month^{-1})	The number of cyclones within 555-km radius at each grid point. For each grid point, same cyclone is counted only once.
Intensity (CVU)	The mean intensity of the detected cyclones. The intensity is defined as the local maximum of 850-hPa relative vorticity.
Growth rate (CVU day^{-1})	The positive value of intensity difference between ±6 hours.
Decay rate (CVU day^{-1})	The negative value of intensity difference between ±6 hours.
Cyclolysis (# month^{-1})	The last point of the detected cyclones (or the location where ETC intensity becomes weaker than 1 CVU).
Lifetime (day)	The time span from cyclogenesis to cyclolysis.
Speed (km h^{-1})	The distance that each cyclone traveled in each time step divided by 6 hours.
Traveling distance (10^3 km)	The traveling distance of cyclone that maintains a minimum intensity of 1 CVU.

2.4 ETC-related precipitation detection

Precipitation associated with ETC is detected using ETC precipitation detection algorithm proposed by Kim et al. (2023). This algorithm define a cyclone zone of a given ETC as the area with relative vorticity over 1 CVU and detect precipitation inside the cyclone zone which is greater than or equal to threshold (5 mm day^{-1} in this study).

After then, the threshold-satisfied neighboring precipitation continue to be detected until there is no precipitation larger than the threshold. It allows to consider local precipitation not only within a ETC but also along their trailing cold front. It is different to other ETC precipitation detecting algorithm using a fixed radial cap method which detect only precipitation within a fixed radius of influence of a ETC. More detailed description of this ETC precipitation detecting algorithm is shown in Kim et al. (2023).

2.5 Model configuration in idealized model experiment

The idealized GCM based on Global/Regional integrated Model system (GRIMs; Hong et al. 2013), version 4.0 is a hydrostatic primitive equation model with a horizontal resolution of T126 and 30 hybrid sigma-pressure vertical levels. The idealized GCM solves the primitive equation using spherical harmonics dynamic core of GRIMs. The horizontal diffusion with the fourth order of diffusion is applied near the model top (3 hPa). No topography is included at the bottom, and no surface friction is considered.

For simplicity, other parameterizations–except large scale condensation–are switched off in our experiment, including surface boundary layer turbulence, cloud microphysics, and radiation. Even though the choice makes our experiment unrealistic, it allows for

examining the role of latent heating by resolved-scale condensation in the evolution of ETC.

The model initialization is based on the idealized dry and moist baroclinic wave tests developed by the Dynamical Core Model Intercomparison Project (DCMIP; Jablonowski and Williamson 2006). The initial conditions include a zonally symmetric jet profile with a maximum wind speed of 35 m s^{-1} at 45°N. The temperatures are distributed through thermal wind balance. A finite-amplitude zonal wind perturbation with a wind speed of 1 m s^{-1} at maximum jet latitude is added for generating the baroclinic wave. In the case of the moist baroclinic wave test, the moisture profile with maximum relative humidity around 90% and 70% placed in the lower levels of tropics and mid-latitudes. The detailed analytic equations are described in Jablonowski and Williamson (2006).

The simulations are run for 15 days. Figure 2.1 shows the time evolution of surface pressure in the dry control run. First, the development of small amplitude waves begins at six days. Then, the rapid intensification stage of ETCs set in at seven days. After that, the ETCs keep developing rapidly until ten days. After that, wave breaking set in. Thus, we considered ETC strength at seven days as a mature stage of ETC in this study.

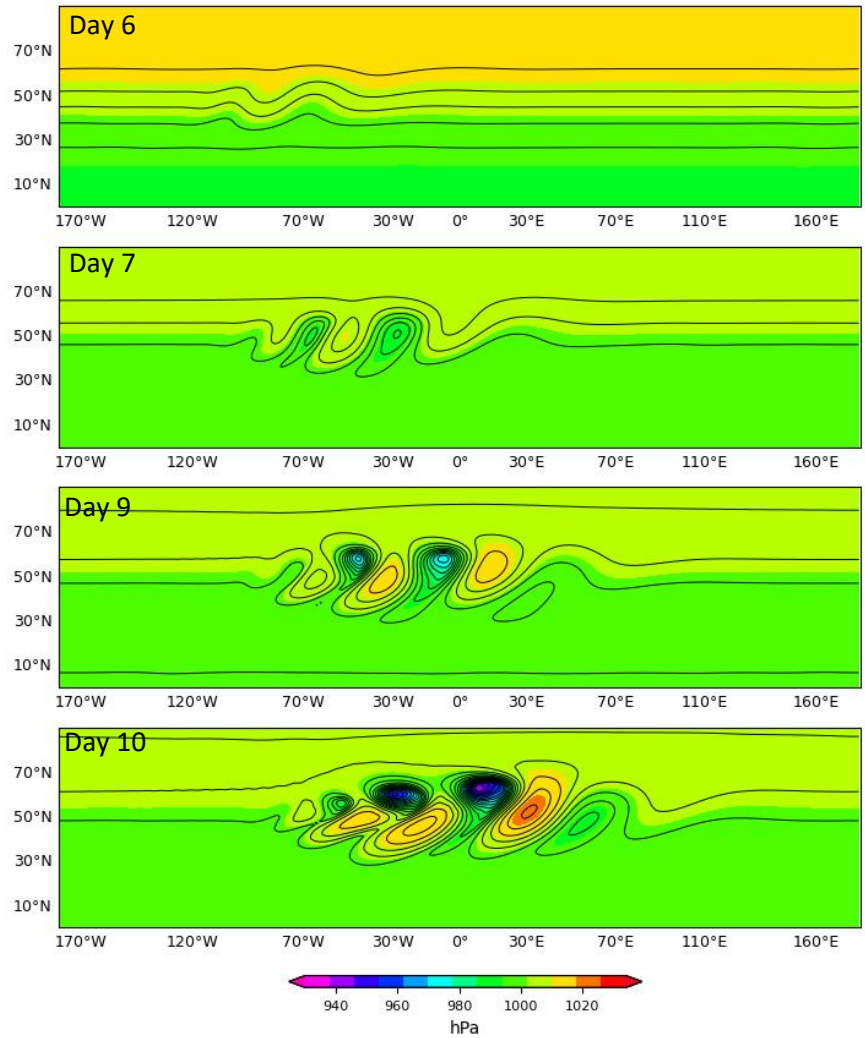

Figure 2.1. Time evolution of baroclinic wave in dry control run. Shadings indicate surface pressure.

2.6 Experimental design in idealized model experiment

We performed six sensitivity experiments that varied two baroclinic components related to ETC development: wind shear and static stability. In Experiment WS, the jet amplitude is modified with the fixed slope of the potential temperature profile in the initial condition. It implies a

change in wind shear. Initial zonal wind perturbation is defined below.

$$u'(\lambda, \varphi, \eta) = Au'_0 cos^{M/2}\eta_v N^{-1} \quad (2.1)$$

where u'_0 indicates the amplitude of u' (6 m s^{-1}), η_v represents $(\eta - \eta_0)/(1 - \eta_0)\,\pi/2$, η is model level, A: the amplitude factor of u', and M: the vertical shape factor of u' (32 for the upper-level u' and 15 for the lower-level u'). The jet amplitude factors between -0.5 and 3.0 are applied in this study. The initial zonal wind perturbation is added to the initial jet profile at all levels to manipulate wind shear, as shown in Fig. 2.2. The maximum speed of initial jet core according to perturbation factors range from 29 to 54 m s^{-1}, in steps of 6 m s^{-1}, with a default of 36 m s^{-1}.

In Experiment ST, the slope of the potential temperature profile is varied with fixed jet amplitude in the initial condition. It indicates a change in static stability. To adjust the vertical profile of the potential temperature, initial temperature perturbation is applied to the initial temperature profile at all levels, as shown below.

$$T'(\lambda, \varphi, \eta) = T_0 \eta^{BR_d\Gamma/g} \quad (2.2)$$

Where T_0 denotes the horizontal-mean temperature at the surface (288 K), R_d is the ideal gas constant for dry air (287.0 J kg^{-1} K^{-1}), g is the gravitational acceleration (9.80616 m s^{-2}), Γ is the temperature lapse rate (0.005 K m^{-1}), and B indicates the amplitude factor of T'. The

multiplicative factors between 0.4 and 1.8 are considered in this study. Consequently, potential temperature added this initial temperature perturbation are shown in Fig. 2.2 and defined as

$$\theta(\lambda,\varphi,\eta) = \langle T(\eta) + T' \rangle \eta^{-\kappa} + 0.75(\pi u_0 / R_d)\, \eta^{1-\kappa} \sin\eta_v \cos^{1/2}\eta_v \times \{(-2\sin^6\varphi(\cos^2\varphi + 1/3) + 10/63) 2u_0 \cos^{3/2}\eta_v + (8/5\cos^3\varphi(\sin^2\varphi + 2/3) - \pi/4) a\Omega\} \quad (2.3)$$

The simultaneous changes in jet amplitude and slope of potential temperature are applied to Experiment WS_ST. It means adjustments of two baroclinic components. Some in the dry simulations of these experiments are denoted as Experiment DRY_WS, DRY_ST, and DRY_WS_ST; others in the moist simulation are represented as MOI_WS, MOI_ST, and MOI_WS_ST.

The idealized GCM based on Global/Regional integrated Model system (GRIMs; Hong et al. 2013), version 4.0 is a hydrostatic primitive equation model with a horizontal resolution of T126 and 30 hybrid sigma-pressure vertical levels. The idealized GCM solves the primitive equation using spherical harmonics dynamic core of GRIMs. The horizontal diffusion with the fourth order of diffusion is applied near the model top (3 hPa). No topography is included at the bottom, and no surface friction is considered.

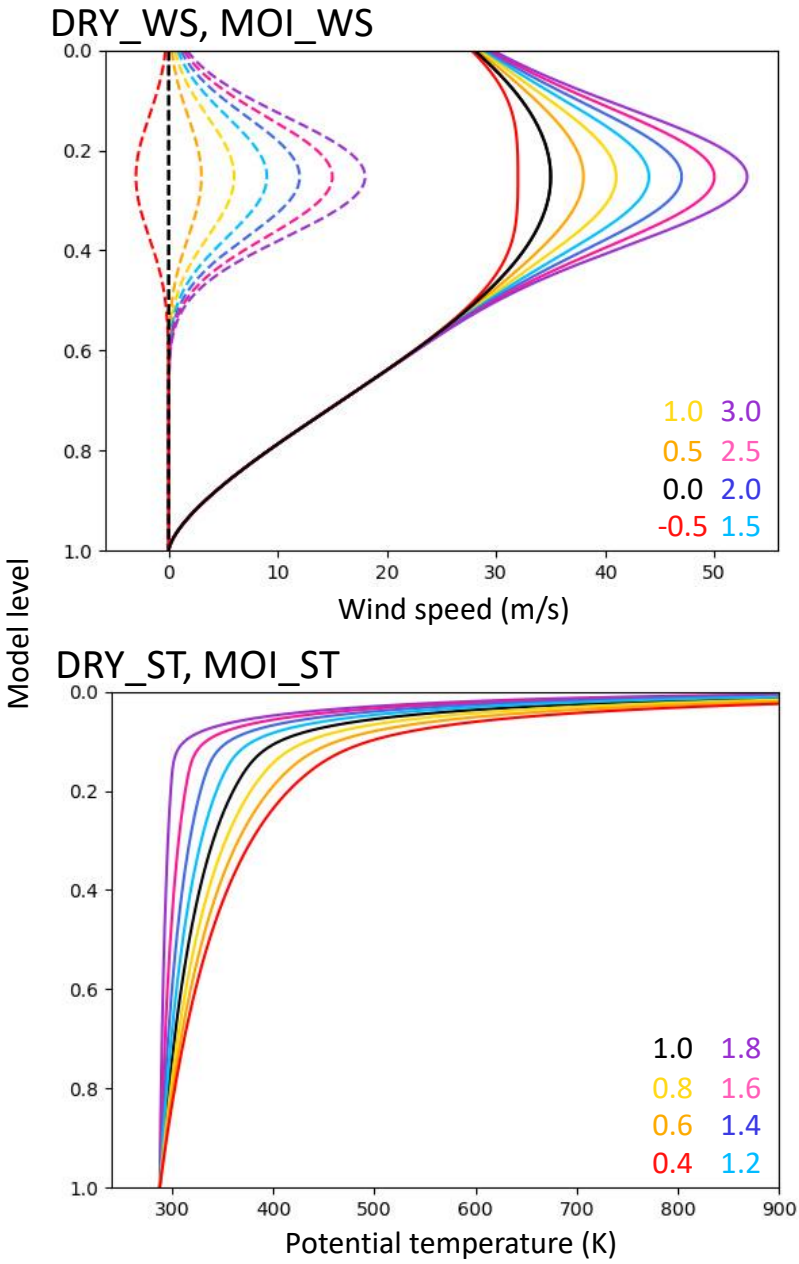

Figure 2.2. Initialized zonal wind and potential temperature profiles for the perturbed parameters in univariate wind shear sensitivity test (top) and univariate static stability sensitivity test (bottom), respectively.

Chapter 3. Extratropical cyclones over East Asia: Climatology, seasonal cycle, long-term trend, and development mechanism

3.1 Climatological baroclinic condition

Figure 3.1a shows the analysis domain. East Asia is characterized by complex topography with the Tibetan Plateau (~30°N) and the Altai–Sayan Mountains (~45°N) in the west and the open ocean in the east. Over the continent, the thick black contour denotes the 1.5-km topography. Although it is not shown, this contour corresponds to surface pressures of approximately 850 hPa. It implies that ETC tracking based on the 850-hPa relative vorticity is not reliable in regions where the topography exceeds approximately 1.5-km altitude.

In the open ocean, SST exhibits a sharp meridional gradient along the Kuroshio–Oyashio Extension (shaded in Fig. 3.1a). Although it is relatively weak, a strong SST gradient also appears in the East Sea/Sea of Japan. These SST gradients are responsible for the strong westerly jet in the upper troposphere through the thermal wind balance (Fig. 3.1b). Many weather systems developing in East Asia travels eastward along this jet. Here, it is noteworthy that East Asia is located at the entrance region of the jet. In terms of synoptic meteorology, the equatorward side

of jet entrance is dominated by ascending motion (Uccellini and Kocin 1987). This may enhance ETC development across South China and possibly enhance lee cyclogenesis in downstream region of the southern Tibetan Plateau.

Figure 3.1c illustrates the Eady growth rate (Eady 1949) that could explain the baroclinic development of ETCs. Although this property is based on linear dynamics and is typically applied to zonal-mean flow, it is still useful for understanding developing mid-latitude weather systems. The Eady growth rate, σ, is defined as

$$\sigma = 0.31\, f\, |\partial u/\partial z| N^{-1}, \tag{3.1}$$

where f is the Coriolis parameter (in s^{-1}), u is the zonal wind (in m s^{-1}), and N is the Brunt-Väisälä frequency (in s^{-1}). The zonal wind and the potential temperature at 500- and 850-hPa pressure levels are used to compute σ.

The Eady growth rate is large over the broad region from the central and northern China to the Kuroshio region due to relatively weak static stability over the continent (not shown) and strong vertical wind shear across the Kuroshio region (Fig. 3.1b). These background conditions may promote lee cyclogenesis around Mongolia and coastal cyclogenesis around the Kuroshio Current (e.g., Chen et al. 1991; Adachi and Kimura 2007; Chen et al. 2014). By considering these background states, the

following subsections describe the climatological characteristics of East Asian ETCs, their seasonality, and long-term trend.

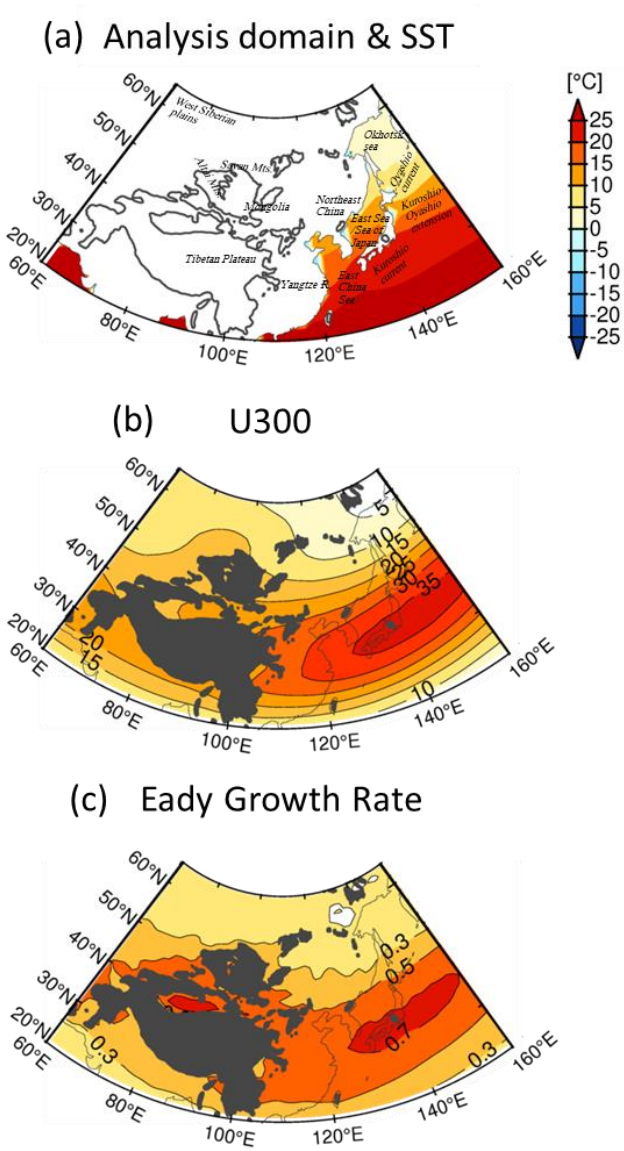

Figure 3.1. (a) Analysis domain and sea surface temperature distribution (shaded; in °C), (b) climatological zonal wind at 300-hPa pressure level (in m s^{-1}), and (c) Eady growth rate (in day^{-1}). The thick line or black shading over the continent indicates 1.5-km high elevation.

3.2 Climatology & development processes

Climatological features of East Asian ETCs are presented in Fig. 3.2. The first three panels show ETC genesis (Fig. 3.2a), frequency (Fig. 3.2b), and intensity (Fig. 3.2c). The other panels show growth (Fig. 3.2d), decay (Fig. 3.2e) rates, cyclolysis (Fig. 3.2f), lifetime (Fig. 3.2g), traveling speed (Fig. 3.2h) and distance (Fig. 3.2i). These properties are shown only at the grid point where ETC frequency is greater than one.

The ETC frequency, as shown in Fig. 3.2a, is pronounced in west Siberia, lee side of mountains, and near the Kuroshio Current. This is consistent with Zhang et al. (2012) who reported that East Asian ETCs typically form over the West Siberian plains, Mongolia, and the coastal regions of East China, then decay in Siberia north of 60°N, northeast China, and the Okhotsk Sea-northwest Pacific region.

The ETC frequency is maximum over the West Siberian Plain. These ETCs, however, are not analyzed in this study because they are typically decaying systems without noticeable impacts on East Asian weather. Figures 3.2b and c indeed show that West Siberian ETCs are not strong and only a few ETCs are generated in this region. As discussed in Chen and Zhang (1996), ETCs in this region typically begin to grow on the leeward side of the Ural Mountains and travel eastward. They develop rather slowly (Fig. 3.2e) and travel a long distance towards Siberia (Fig.

3.2i) at a relatively fast speed (Fig. 3.2h), then eventually decay at approximately 80°E (Fig. 3.2f). In the course of their life cycle, West Siberia ETCs rarely affect East Asian weather.

The ETCs that affect East Asian weather typically form on the lee side of the Altai-Sayan Mountains and the Tibetan Plateau as well as over the east coast of Japan (Fig. 3.2a). These ETCs develop approximately three to six times per month with a local maximum near Mongolia and the Kuroshio region (Fig. 3.2b). The detected ETCs are relatively strong with mean intensity ranging from two to five CVU, with increasing intensity from the continent to the open ocean (Fig. 3.2c).

The growth rate of East Asian ETCs is typically larger than 1.6 CVU per day with a distinct maximum over the Kuroshio region (Fig. 3.2d). Most ETCs decay over the Okhotsk Sea with a maximum decay rate of more than -1.2 CVU per day (Fig. 3.2e). On average, ETCs are sustained for approximately five days (Fig. 3.2g) and travel more than 4,000 km in mid-latitudes at a speed of about 40 km per hour (Figs. 3.2h, i).

Among the three cyclogenesis regions (Fig. 3.2a), ETCs form most frequently in downstream region of the Altai–Sayan Mountains. These ETCs, which are referred to as Mongolia ETCs in this study (box “A” in Fig. 3.2b), are not as strong as West Siberia ETCs (Fig. 3.2b), but they are newly formed cyclones (Fig. 3.2c) that grow quickly over time (Fig. 3.2e).

Chen and Lazić (1990) showed that Mongolia ETCs are often initiated by a cutoff low. When a mid-tropospheric trough sweeps past the northern region of the Altai-Sayan Mountains, it rapidly develops and turns into a cutoff low within one to two days. The induced surface cyclones slowly move towards northeast China and the East Sea (Fig. 3.2h) and then rapidly intensify over the ocean (Figs. 3.2b and e) presumably due to moisture supply and strong baroclinicity (Hirata et al. 2015).

The individual tracks of Mongolia ETCs are further illustrated in Fig. 3.3a. Most ETCs are relatively weak over the continent (blue color) but become stronger over the open ocean (red color). They travel not only eastward but also southeastward or northeastward. When traveling southeastward in spring, they can transport Asian dust from Mongolia and North China to the downstream region (e.g., Lee et al. 2016; Jung et al. 2019).

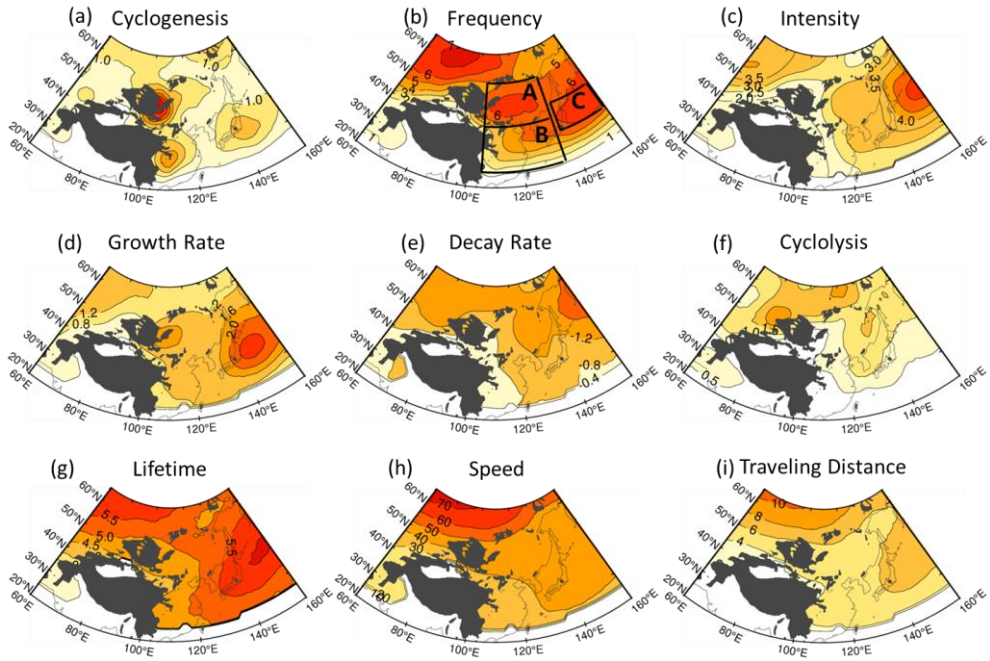

Figure 3.2. Climatology of East Asian ETCs: (a) cyclogenesis (in # month^{-1}), (b) frequency (in # month^{-1}), (c) intensity (in CVU), (d) growth rate (in CVU day^{-1}), (e) decay rate (in CVU day^{-1}), (f) cyclolysis (in # month^{-1}), (g) lifetime (in day), (h) speed (in km h^{-1}), and (i) traveling distance (in 10^3 km). See Table 2.3 for the definition and unit of each property. All ETC properties are only considered for the grid points where one or more ETCs are present. Three black boxes in (b) represent (box A) Mongolia, (box B) South China, and (box C) Kuroshio Current domain.

The second dominant cyclogenesis is found on the leeward side of the southern Tibetan Plateau (Fig. 3.2a). The ETCs in this region are referred to as South China ETCs (box "B" in Fig. 3.2b). As illustrated in Fig. 3.3b, they travel eastward or northeastward towards the East China Sea and then to the Kuroshio region. Similar to Mongolia ETCs, South China ETCs grow rapidly over the ocean (Fig. 3.2d). This result again suggests

that the warm ocean plays a crucial role in the development of East Asian ETCs.

Figure 3.2a further reveals that the Kuroshio region is a central region for coastal cyclogenesis. The ETCs in this region travel along the Kuroshio Current (Fig. 3.2b) and grow rapidly at the Kuroshio-Oyashio Extension (Figs. 3.2c and d). These cyclones, hereafter referred to as Kuroshio ETCs, develop by baroclinic instability and diabatic heating (Hirata et al. 2015). As shown in Fig. 3.3c, Kuroshio ETCs do not always travel eastward along the jet. Many of them also travel northward or northeastward across the jet. These northward-traveling cyclones typically grow more rapidly than those traveling eastward (Hayasaki et al. 2013).

The results shown in Figs. 3.2 and 3.3 suggest that East Asian ETCs typically form on the leeward side of the Altai–Sayan Mountains (Mongolia ETCs), the Tibetan Plateau (South China ETCs), and over the Kuroshio region (Kuroshio ETCs), and travel eastward reaching maximum intensity around the Kuroshio–Oyashio Extension. Although ETCs move and grow rather slowly over the continent, they travel faster and become stronger over the ocean. The lifetime of ETCs also becomes longer over the ocean. Most ETCs tend to decay over the Okhotsk Sea (Fig. 3.2f) where SSTs are low (Fig. 3.1a).

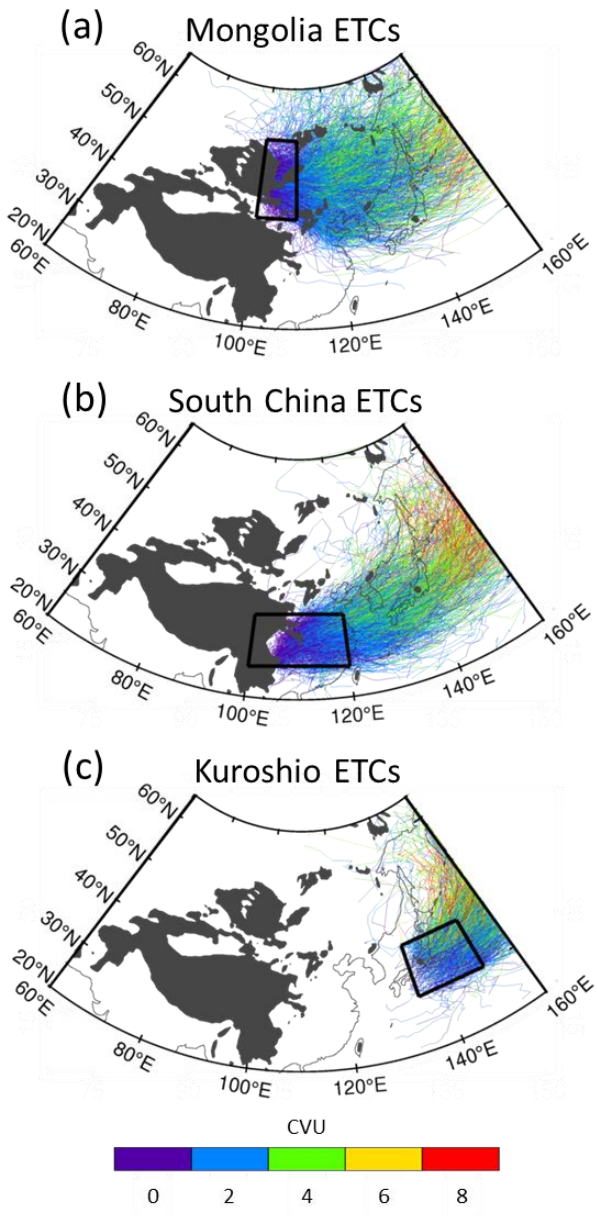

Figure 3.3 Individual ETC tracks that start from the leeward sides of (a) the Altai–Sayan Mountains and (b) the Tibetan Plateau, and (c) from the Kuroshio Current region. The color represents ETC intensity in CVU. The black box in each plot indicates the domain where the initial ETCs are located.

3.3 Seasonality

Figures 3.4–3.6 present the seasonal cycle of East Asian ETC properties. ETC statistics have experienced seasonal variations over East Asia. The seasonal cycles of ETC frequency and intensity, as examples, are more clearly presented in Fig. 3.7 and Table 3.1 for Mongolia, South China, and Kuroshio ETCs.

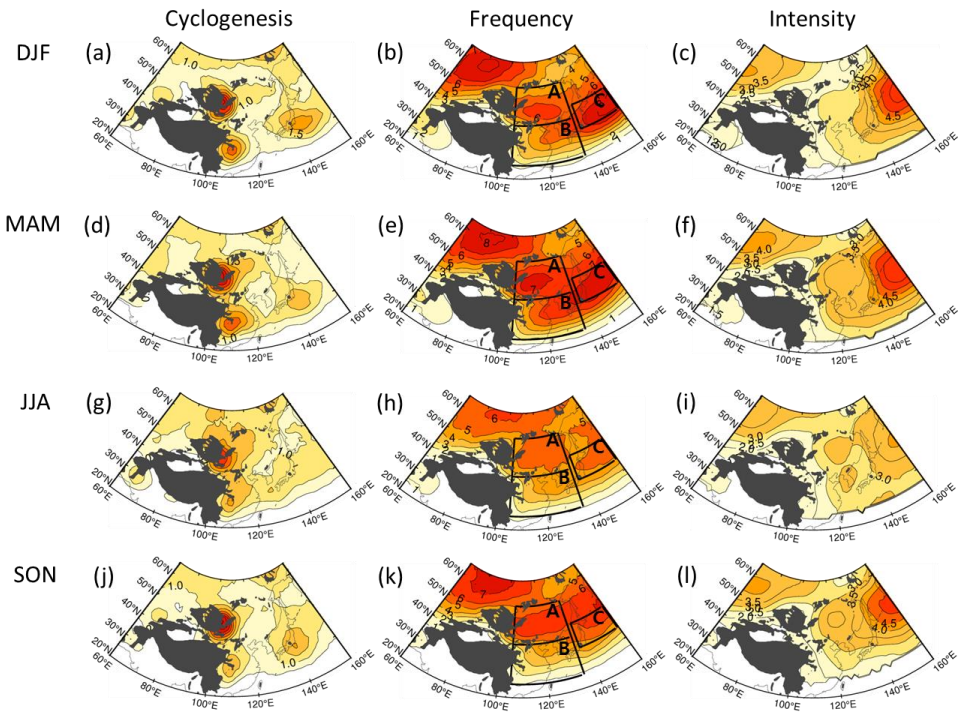

Figure 3.4. Same as Figs. 3.2a–c but for (first) winter, (second) spring, (third) summer, and (fourth row) fall.

The left column of Fig. 3.4 reveals that cyclogenesis in East Asia is almost stationary throughout all seasons. The three major regions of

cyclogenesis (i.e., the downstream region of the Altai-Sayan Mountains, the southern Tibetan Plateau, and over the Kuroshio region) are robustly found in all seasons. Only the number of generated ETCs changes with seasons in each region.

Cyclogenesis is typically maximum in winter (or extended winter) but minimum in summer. Such seasonality is evident over the Kuroshio region. However, continental ETCs exhibit subtle differences between northern and southern China. The ETC genesis in the downstream region of the Altai-Sayan Mountains is more frequent in fall (SON) than in summer (JJA). However, that of the southern Tibetan Plateau shows an opposite seasonality with slightly more frequent cyclogenesis in summer than in fall (compare Figs. 3.4g and j). This result suggests that the continental ETCs in northern and southern China may have different development processes. Kang et al. (2020) indeed showed that while Mongolia ETCs develop dynamically through the vertical coupling, South China ETCs develop with intense diabatic heating.

The middle column of Fig. 3.4 displays the frequency of ETCs in each season. Although the exact locations of Mongolia, South China, and Kuroshio ETCs are slightly different across the seasons, their existence is prominent. The frequency peaks move slightly equatorward from summer to winter along with an equatorward shift of the westerly jet. Its

seasonality, however, is not monotonic in seasons. For instance, Mongolia ETCs are most frequent in spring (Fig. 3.4e) and fall (Fig. 3.4k). Their frequencies are even higher than the winter ETC frequency (Fig. 3.4b). This bimodal seasonality is concisely summarized in Fig. 3.7a and Table 3.1. The springtime ETC frequency is approximately 1.1 cyclones per month higher than the wintertime ETC frequency. This difference is approximately 20% of the total wintertime ETC frequency over Mongolia (Table 3.1). Although less pronounced, ETC frequency over South China is also maximum in spring (Fig. 3.4b). Quantitatively, South China ETCs are observed approximately 4.8 times per month in the spring but only approximately 4.0 times per month in the winter (Fig. 3.7b and Table 3.1). They are however not frequent in fall. Figure 3.4k shows that South China ETCs are not well defined in fall (i.e., no local maxima around box B). This result again suggests that two continental ETCs (i.e., Mongolia and South China ETCs) are not likely organized by the same physical processes.

The Kuroshio ETCs are most pronounced in both winter and spring (about to eight ETCs per month) but least in summer (about to five ETCs per month). This seasonality, as summarized in Fig. 3.7c, is largely explained by the seasonal march of local baroclinicity in the region (Lambert 1996; Graham and Diaz 2001). Here it is noteworthy that local cyclogenesis is much smaller than total ETC frequency. The Kuroshio

ETCs are locally generated approximately two cyclones per month in winter (Fig. 3.4a), and one cyclone per month in summer (Fig. 3.4g). These numbers imply that only 21–30% of ETCs in this region is locally generated, and the majority of ETCs in this region are simply the ones traveling from the continent.

The rightmost column of Fig. 3.4 shows the seasonal distribution of ETC intensity. As shown in the annual climatology, the maximum intensity appears over the Kuroshio–Oyashio Extension in all seasons. While its seasonality is somewhat similar to that of ETC frequency (compare the middle and right columns in Fig. 3.4), there is an important difference. Unlike the ETC frequency, ETC intensity is the strongest in spring for all regions (Fig. 3.4f) and it is different from the seasonality of ETC frequency, which depends on the region. The maximum intensity for South China and Mongolia ETCs is approximately 3.0–3.3 CVU in spring, and this is approximately 0.4–0.7 CVU (about 15–27% of the total wintertime cyclone intensity) stronger than that of wintertime ETCs (Figs. 3.7a and b). Even in the Kuroshio region, spring ETCs are slightly stronger than winter ETCs (Figs. 3.4c and f). This seasonality can be explained by the concept from the midwinter suppression of the Pacific storm track (Nakamura 1992).

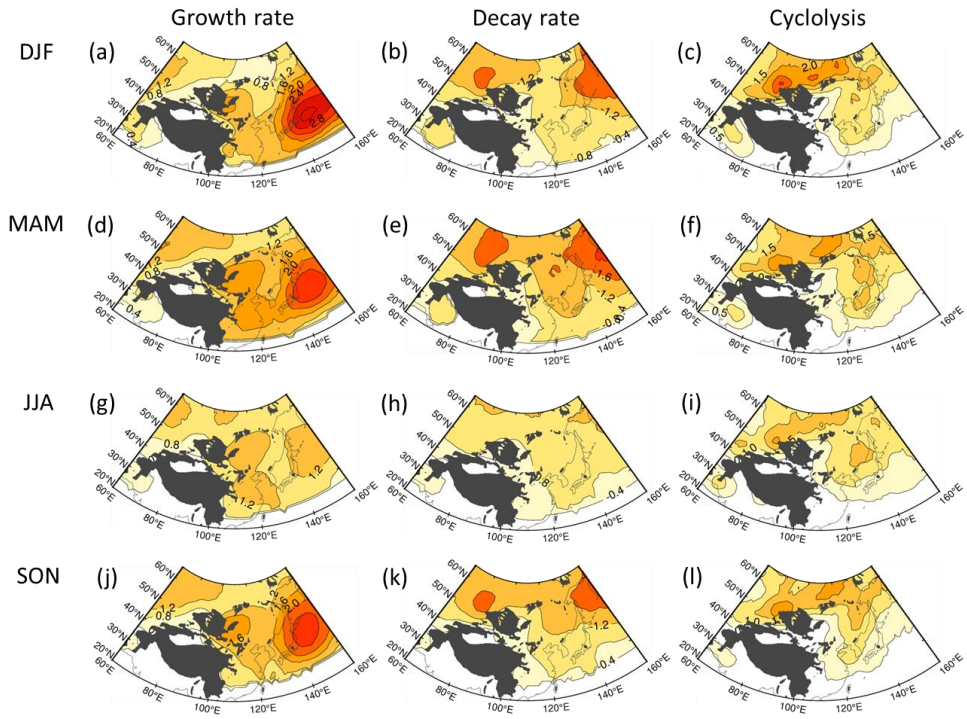

Figure 3.5. Same as Figs. 3.2d–f but for (first) winter, (second) spring, (third) summer, and (fourth row) fall.

Figure 3.5 further illustrates ETC growth rate (left), decay rate (middle), and cyclolysis (right) in each season. Similar to climatology (Fig. 3.2d), growth rate is high over Mongolia, Yangtze River, and the Kuroshio-Oyashio extension (Figs. 3.5a, d, g, and j). East Asian ETCs grow fastest over the Kuroshio-Oyashio extension, slightly upstream of maximum ETC intensity (Figs. 3.4c, f, and i). Their growth rate is maximum in winter (greater than 3.1 CVU per day) when SST is relatively warm, and its meridional gradient is sharp, but minimum in summer (about 1.3 CVU per day). Around Mongolia, ETCs grow faster in spring (higher than 1.6

CVU per day) than in summer (about 1.3 CVU per day). Although growth rate is also high in fall and winter, the region of high growth rate is narrow. The South China ETCs typically strengthen around Yangtze River with a maximum growth rate in spring but a minimum rate in fall as in cyclogenesis (Figs. 3.4a, d, g, and j).

The decay rate is further illustrated in Figs. 3.5b, e, h, and k. Overall decay rate is high in the Okhotsk Sea, downstream of the rapid ETC growth region (compare the left and middle columns in Fig. 3.5). This indicates that rapidly developing ETCs over the Kuroshio–Oyashio Extension tend to decay over the cold ocean as they travel northeastward. However, only few ETCs die in this region. As shown in the rightmost column of Fig. 3.5, cyclolysis mainly occurs along the coastline of the continent rather than over the cold ocean. The dying ETCs in this region, maximum of 1.5 cyclones per month, are typically those traveling in the continent or those landing from the ocean.

Figure 3.6 presents the seasonal evolution of ETC lifetime, traveling speed and distance. It is found that winter ETCs have a relatively short lifetime, moving fast over the ocean. The summer ETCs, although weak and less frequent, are maintained one or two days longer than the winter ETCs in most regions. Moreover, they travel slowly (about 30 km per hour) because of weak background flow. Most ETCs travel more than 4,000 km

in the analysis domain.

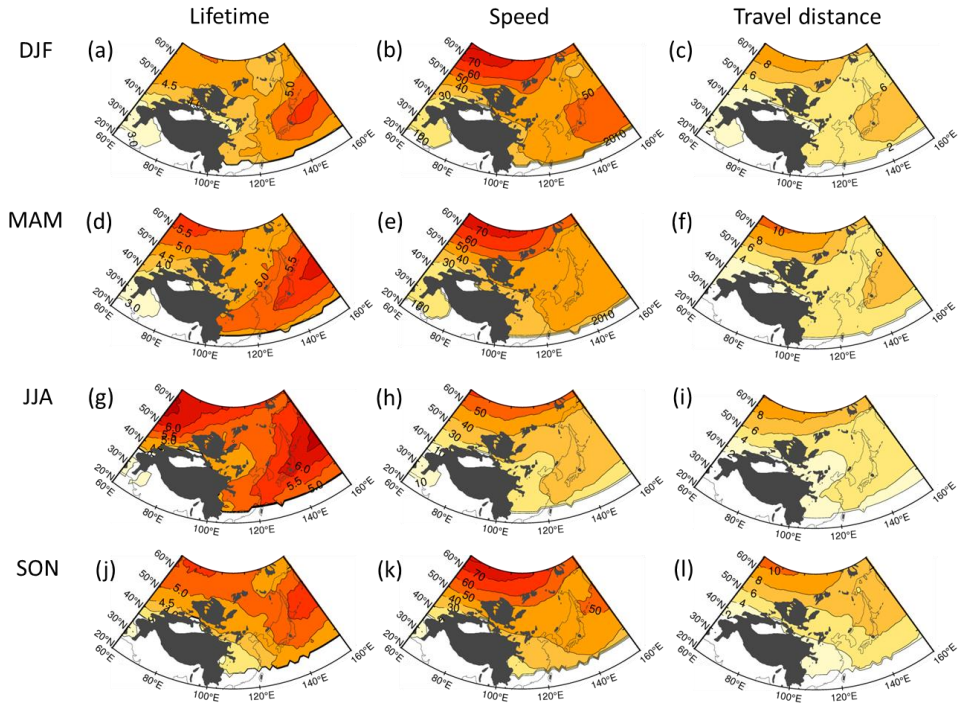

Figure 3.6. Same as Figs. 3.2g–i but for (first) winter, (second) spring, (third) summer, and (fourth row) fall.

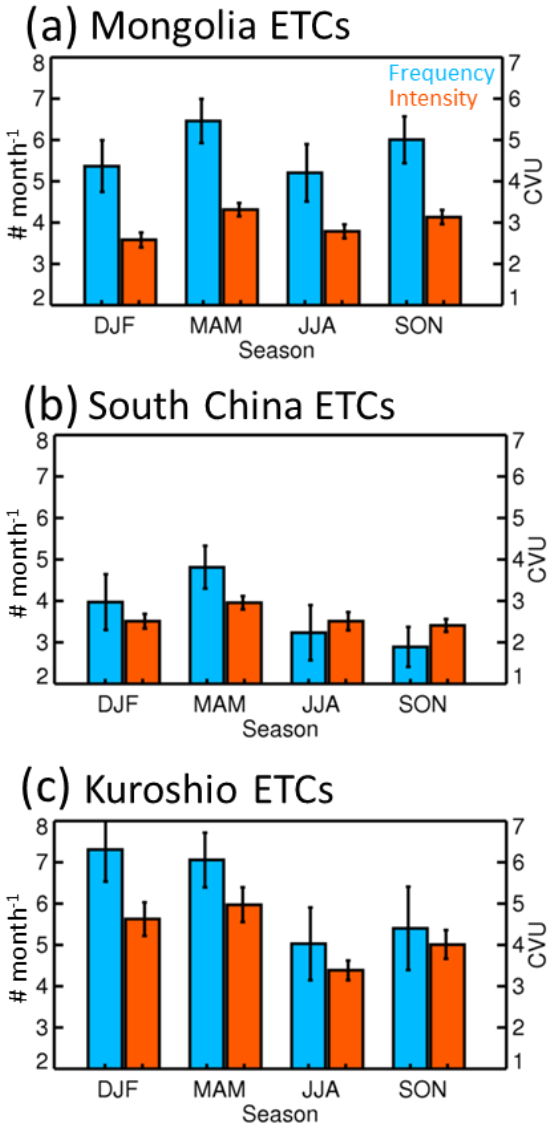

Figure 3.7. Long-term mean Seasonal cycle of ETC frequency (blue bars) and intensity (orange bars) in the three cyclogenesis regions shown in Fig. 3.2a. The error bar indicates the interannual variation at one standard deviation.

3.4 Long-term variability

The above result reveals that East Asian ETCs have different climatic features depending on the season and region. Although not examined in detail, they also exhibit considerable temporal variability. Table 3.1 concisely summarizes the interannual variability of ETC frequency. The number of East Asian ETCs varies about 10–20% from one year to another. The largest variability, which is observed for Kuroshio ETCs in fall, is about one cyclone per month.

Table 3.1. The long-term mean and interannual variability (one standard deviation) of seasonal ETC frequency over Mongolia, South China, and the Kuroshio Current region. Long-term trend is indicated in parenthesis. The trend that is statistically significant at the 95% confidence level is denoted with an asterisk.

	Mongolia ETCs	South China ETCs	Kuroshio ETCs
DJF	5.37±0.62 (0.01 dec^{-1})	3.97±0.67 (-0.14 dec^{-1})	7.31±0.78 (-0.13 dec^{-1})
MAM	6.46±0.53 (-0.01 dec^{-1})	4.81±0.52 (-0.16* dec^{-1})	7.06±0.66 (-0.03 dec^{-1})
JJA	5.20±0.69 (-0.27* dec^{-1})	3.23±0.66 (0.00 dec^{-1})	5.03±0.88 (-0.06 dec^{-1})
SON	6.00±0.57 (-0.11 dec^{-1})	2.89±0.48 (-0.06 dec^{-1})	5.40±1.01 (0.01 dec^{-1})

Figure 3.8 presents the long-term trends of ETC frequency (see also the parenthesized number in Table 3.1). East Asian ETCs show slightly negative trends in most seasons and most regions. However, their trends are largely statistically insignificant. Two exceptions are springtime South China ETCs (blue shading in Fig. 3.8b) and summertime Mongolia ETCs (Fig. 3.8c). Their trends, -0.16 and -0.27 cyclones per decade, are marginally significant at the 95% confidence level (Table 3.1). These numbers correspond to about 3.3% and 5.2% reduction of ETC frequency per decade in each region. Such changes are mainly due to reduced cyclogenesis (not shown). Although not shown, the overall intensities of these ETCs do not change much.

Figure 3.9 further shows the time series of the springtime South China ETC frequency and the summertime Mongolia ETC frequency. The top-50% ETCs in intensity are also separately shown. It turns out that only relatively weak ETCs have decreased over South China (Fig. 3.9a). The top-50% ETCs show essentially no trends, indicating that large-scale circulation changes may have different impacts on weak and strong ETCs. Unlike South China ETCs, Mongolia ETCs have systematically decreased over the analysis period (Fig. 3.9b).

What causes declining trends in ETC frequency? Cho et al. (2018)

argued that the reduction in South China ETC frequency is partly caused by weakened moisture flux convergence in response to enhanced warm-pool convection over the last 39 years. Note that the Gill-type response (Gill 1980) to the enhanced tropical convection results in strengthened moisture flux convergence over southeast China and the South China Sea, but weakened moisture flux convergence over southwest China where South China ETCs develop. This argument is partly supported by the nature of South China ETCs. Kang et al. (2020) showed that South China ETCs are typically shallow in the vertical and not well coupled with an upper-level trough. These ETCs grow with intense diabatic heating in the mid-to-lower troposphere, possibly due to moisture supply from the East China Sea.

Unlike South China ETCs, the long-term trends of summertime Mongolia ETCs are not well addressed in the literature. It is particularly true for observations. By performing coupled model experiments, Loptien et al. (2008) showed that summertime ETC frequency over Mongolia would decrease under future climate scenarios. However, the driving mechanisms have not been identified.

It is anticipated that ETC-frequency trends, shown in Fig. 3.8, are at least partly caused by the long-term changes in atmospheric circulation. To better understand declining ETC frequency in East Asia, the long-term

trends in jet (zonal wind at 300 hPa) and static stability, which are essential factors for baroclinic instability, are examined in Fig. 3.10. The springtime jet does not show any significant trends (Fig. 3.10a). Although weak negative trends are observed in summer, the trends in the downstream region of the Tibetan Plateau are confined to the narrow regions (Fig. 3.10b). This result suggests that ETC-frequency changes are not likely associated with vertical wind shear changes.

Figures 3.10c and d show the bulk stability changes in the two seasons. The bulk stability is computed by potential temperature difference between 300- and 700-hPa pressure levels. In spring, bulk stability has significantly increased in the subtropics from northern India to southern Japan (Fig. 3.10c). The stability has also increased in summer but mostly in northern China (Fig. 3.10d). These regions of enhanced stability, presumably due to global warming, coincide with those of reduced ETC frequency, indicating that ETC activity changes in East Asia are partly associated with background state changes. To better understand the physical mechanism(s), further investigations especially using numerical model would be needed.

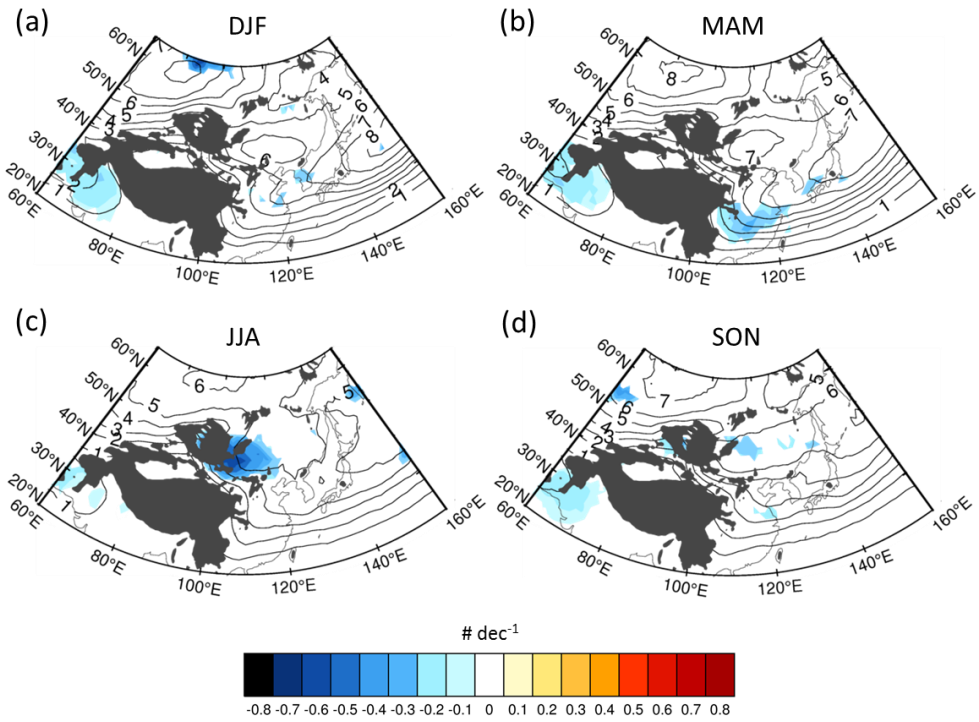

Figure 3.8. Seasonal-mean ETC frequency (contours; identical to the middle column of Fig. 3.4) and its long-term trend (shaded; in number of ETCs per decade). Only trends that are statistically significant at the 95% confidence level are shown.

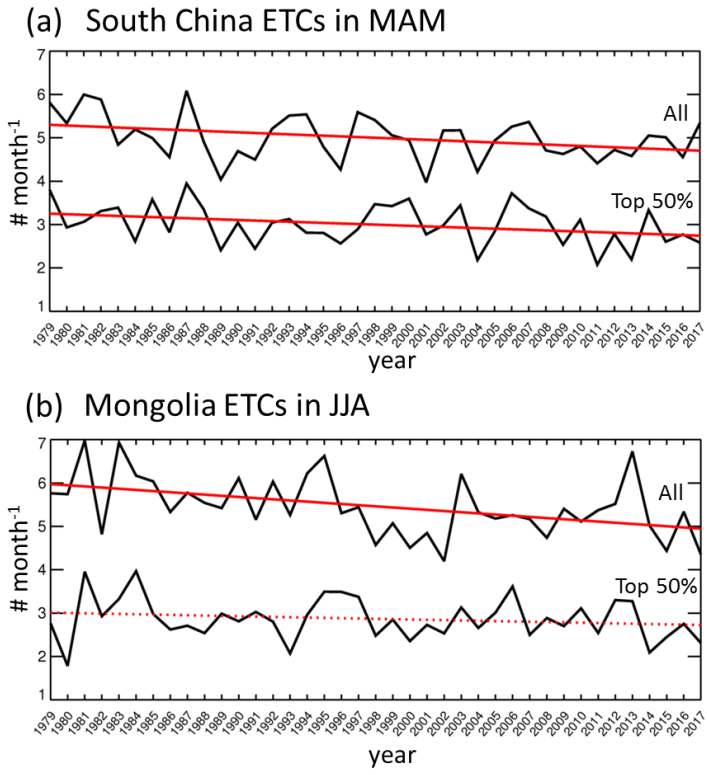

Figure 3.9. Time series of ETC frequency and its linear trend for (a) springtime South China ETCs and (b) summertime Mongolia ETCs over the period of 1979–2017. Top 50% ETCs in intensity are separately shown. The solid red lines indicate statistically significant trends at the 95% confidence level.

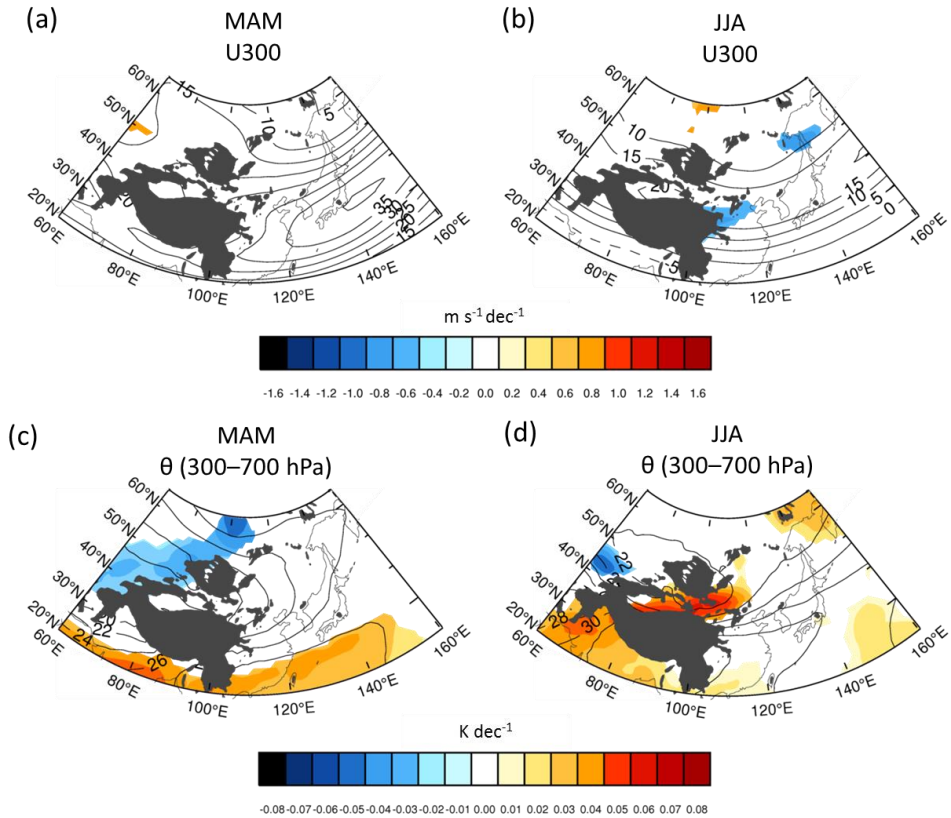

Figure 3.10. Seasonal-mean (contours) and decadal trends (shaded) of 300-hPa zonal wind (top; in m s^{-1} dec^{-1}) and bulk static stability (bottom; in K dec^{-1}) in spring (left) and summer (right). Bulk static stability is defined by potential temperature difference between at the 300- and 700-hPa pressure levels. The trends that are statistically significant at the 95% confidence level are denoted with dots.

Chapter 4. East Asian cyclone changes in future climate

4.1 Evaluation of the historical CMIP5 and 6 simulations

Figure 4.1a shows the climatological ETC frequency over the East Asian domain, including two major mountains (i.e., the Tibetan Plateau and Altai-Sayan Mountains north of the Plateau in Fig. 4.1a), in reanalysis. The ETC frequency is pronounced over the West Siberian Plain. Many ETCs in this region form in the downstream region of the Ural Mountains and travel eastward, then decay in the upstream region of the Altai-Sayan Mountains (Lee et al. 2020). The ETC frequency is also pronounced in the downstream regions of the Altai-Sayan Mountains and the Tibetan Plateau. Most of continental ETCs form in these regions (Fig. 4.2a). The continental ETCs travel eastward and rapidly intensify when passing over the ocean (Fig. 4.1a; Lee et al. 2020). The oceanic ETCs are mainly generated south of Japan (Fig. 4.2a) and travel along the Kuroshio-Oyashio extension (Fig. 4.1a).

The spatial distribution of ETC frequency is qualitatively well reproduced by the CMIP5 models (Figs. 4.1b–j). Nevertheless, there are still systematic biases. Most models overestimate continental ETC frequency around the Altai-Sayan Mountains (see red shading), with

BCC-CSM1-1-m, BNU-ESM, and NorESM1-M exaggerating ETC frequency over the high terrain regions from the Tibetan Plateau to the Altai-Sayan Mountains (Figs. 4.1b, c, and j) but underestimate ETC frequency along the Kuroshio-Oyashio extension where sea surface temperature sharply changes in latitude. All models also underestimate ETC frequency in the West Siberian Plain. These biases are largest in NorESM1-M, underestimating East Asian ETC frequency by almost 30% less than the reanalysis data (Fig. 4.1j).

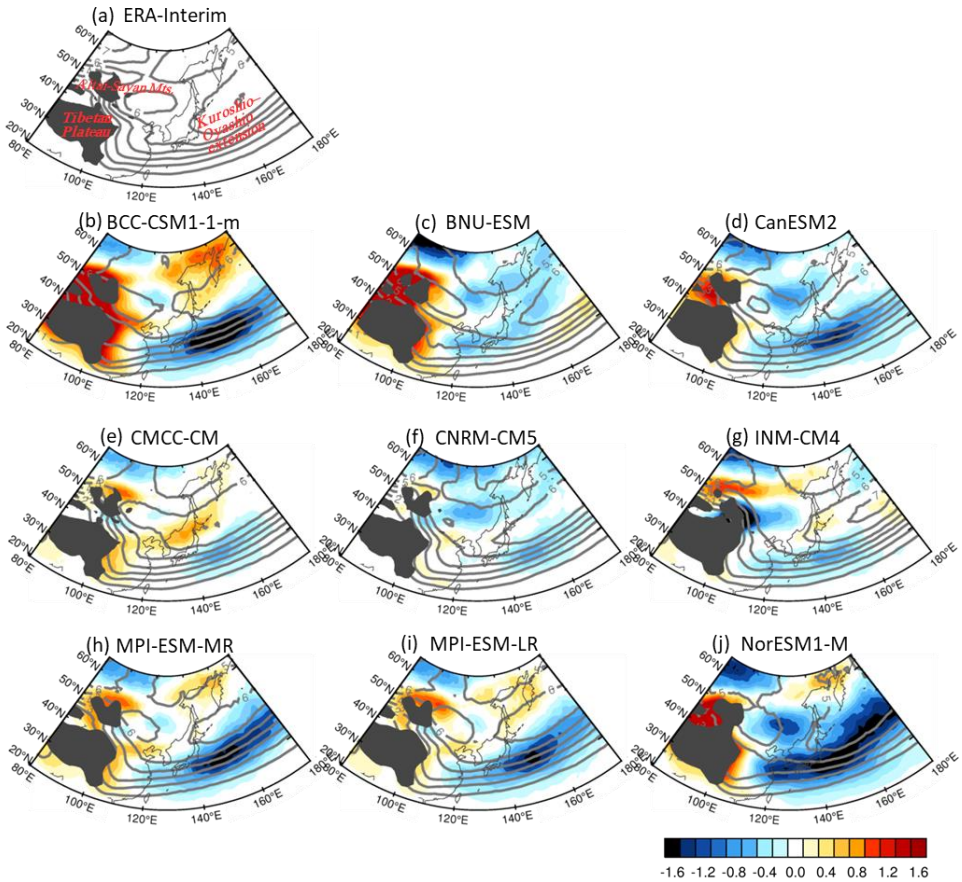

Figure 4.1. ETC frequency (contours; # $\mathbf{month^{-1}}$) in (a) ERA-Interim, (b–j) nine CMIP5 models with model biases (shaded). The dark gray mask indicates a 1.5-km high elevation.

The climatological cyclogenesis is illustrated in Figure 4.2. The lee cyclogenesis downstream of the Altai-Sayan Mountains and the Tibetan Plateau as well as cyclogenesis along the Kuroshio-Oyashio extension (Fig. 4.2a) are qualitatively well captured by the models (Figs. 4.2b–j). However, most models underestimate lee cyclogenesis downstream of the mountains and ETC development in the south of Japan. The three

models (BCC-CSM1-1-m, BNU-ESM, and NorESM1-M) having the large biases in ETC frequency not only underestimate lee cyclogenesis but also exaggerate cyclogenesis over the high terrain regions (Figs. 4.2b, c, and j). It is noteworthy that INM-CM4 exhibits a southward shifted lee cyclogenesis downstream of the Altai-Sayan Mountains (see red shading in Fig. 4.2g). This bias partly results from the misrepresentation of mountains which are biased southward (see terrain mask in Fig. 4.2g). However, the biases over the high terrain regions and those on its downstream regions in most other models (e.g., BCC-CSM1-1-m, BNU-ESM, and NorESM1-M) cannot be explained by misrepresented topography. Instead, they are likely influenced by the physical parameterizations that determine the complex interactions between the mean flow and topography. Those parameterizations include the boundary layer turbulence scheme, the low-level blocking scheme, and the sub-grid orographic gravity wave drag scheme (Lott and Miller 1997; Beljaars et al. 2004). Simpson et al. (2020) recently showed that the model biases in storm track downstream of mountains could be improved by updating the boundary layer turbulence and low-level blocking schemes. However, the details of such parameterizations in each CMIP5 model are not available, and further studies are needed to identify the precise cause(s) of ETC biases over the high terrain regions.

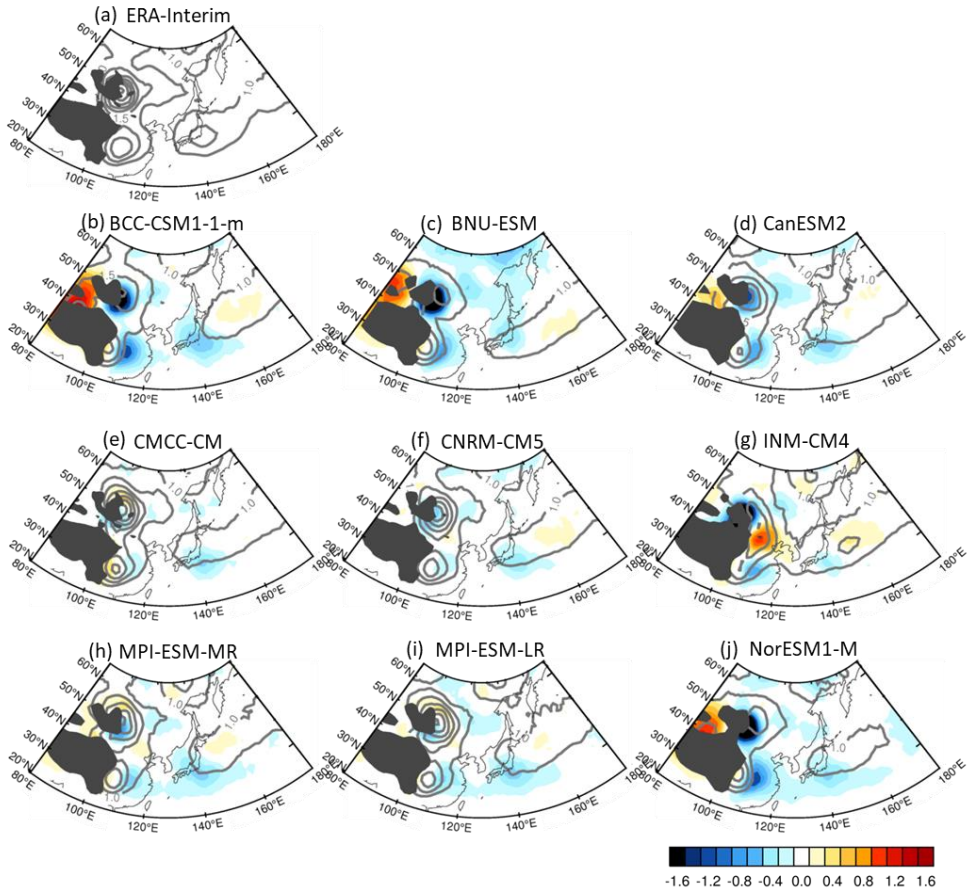

Figure 4.2. Same as Fig. 4.1 but for ETC genesis (# $\mathbf{month^{-1}}$).

The model performance in reproducing the climatological ETC frequency, intensity, and cyclogenesis is summarized in Figure 4.3. All three properties are evaluated over the East Asian domain (80–180°E, 20–65°N) using a Taylor diagram (Taylor 2001). Each diagram illustrates how closely the spatial distribution of the simulated ETC properties (d) matches with the ERA-Interim (r) in terms of the centered root-mean-square error (RMSE; E), the pattern correlation coefficient (R), and the

spatial standard deviation (STD).

$$E = \{\frac{1}{M}\sum_{m=1}^{M}[(d_m - \bar{d}) - (r_m - \bar{r})]^2\}^{\frac{1}{2}}, \quad (4.1)$$

$$R = \frac{\frac{1}{M}\sum_{m=1}^{M}(d_m - \bar{d})(r_m - \bar{r})}{STD_d STD_r}, \quad (4.2)$$

$$STD_d = [\frac{1}{M}\sum_{m=1}^{M}(d_m - \bar{d})]^{\frac{1}{2}}, \quad (4.3)$$

$$STD_r = [\frac{1}{M}\sum_{m=1}^{M}(r_m - \bar{r})]^{\frac{1}{2}}, \quad (4.4)$$

where m is the space index, M is the number of grids, d_m and r_m indicate ETC properties at m^{th} grid in a model and reanalysis data, $\bar{d}$ and $\bar{r}$ denote ETC properties averaged over East Asian domain in a model and reanalysis data, and STD_d and STD_r represent the spatial standard deviations of d and r.

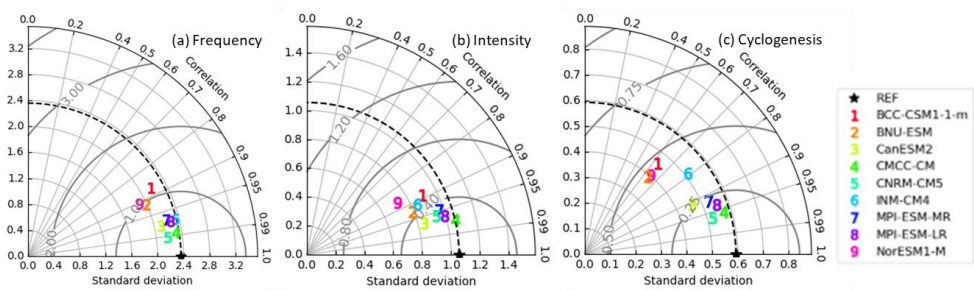

Figure 4.3. Taylor diagrams for climatological (a) ETC frequency, (b) intensity, and (c) genesis over East Asia simulated by each CMIP5 model during 1979–2004.

All nine models show a smaller standard deviation than that of the ERA-Interim. It implies that the CMIP5 models typically underestimate

spatial variations of East Asian ETCs. Among them, five models show relatively high correlation coefficients, low RMSEs, and comparable standard deviations to the ERA-Interim in all three ETC properties than other models. They are CMCC-CM, CNRM-CM5, MPI-ESM-LR, MPI-ESM-MR, and CanESM2. These five models are referred to as the Best5 models below. Note that INM-CM4, which reproduces East Asian ETC frequency reasonably well (Fig. 4.3a), is excluded because of a critical error in cyclogenesis (Fig. 4.3c; see also Fig. 4.2g).

It is natural to ask what determines the Best5 models. One of the key factors is model resolution. All models except CanESM2 have relatively fine grid spacing (Table 2.1). This is consistent with Colle et al. (2013) who reported that the CMIP5 models with a high horizontal resolution tend to have small biases in ETC frequency. However, the model resolution alone does not explain the model bias as CanESM2 has a coarse resolution. Likewise, BCC-CSM1-1-m shows a low performance although its resolution is relatively high.

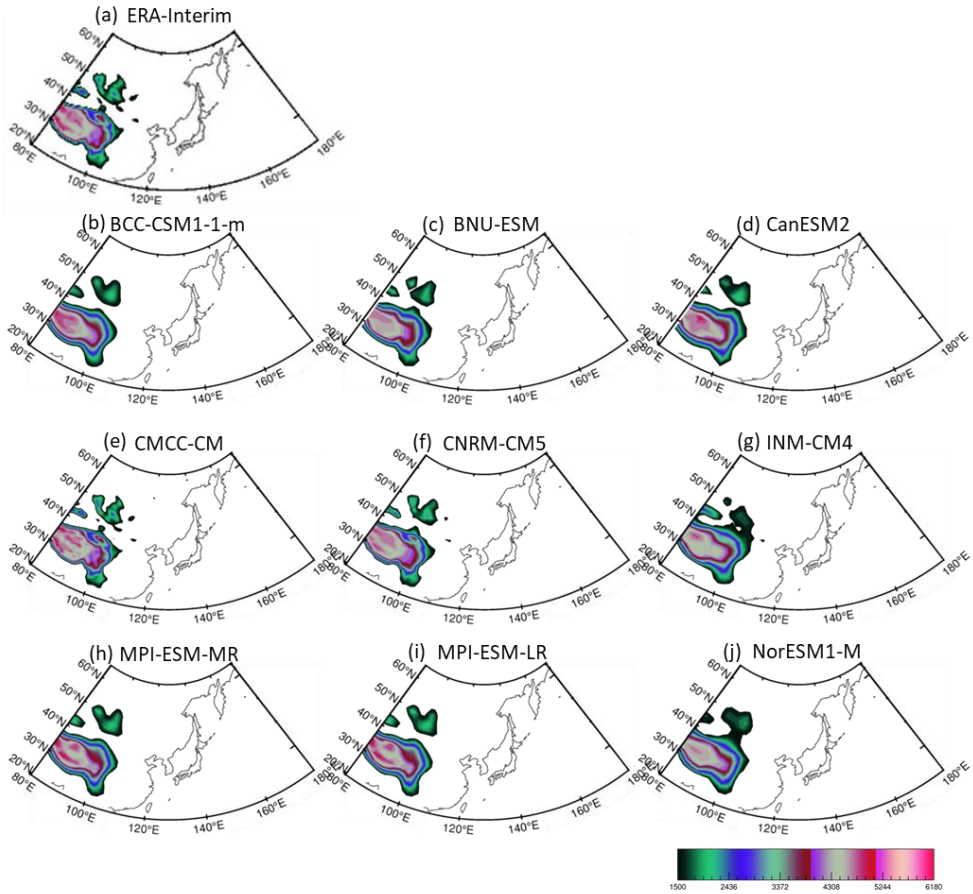

Supplementary figure 1. Topography over 2,000 m in (a) the ERA-Interim and (b–j) nine CMIP5 models. The unit is a kilometer.

As discussed earlier, another key factor that affects continental ETC frequency is the topography. Here, it is important to note that the resolution of the topography is not always equal to the resolution of the model. For instance, BCC-CSM1-1-m whose horizontal grid spacing is 1.1° employs a slightly coarser topography than CanESM2 whose horizontal grid spacing is 2.8° (Figs. 4.1 and 4.2; see also Fig. S1). In Table 2.1, the

complexity of topography is quantified by computing the spatial standard deviation of topography over the East Asian mountain region (80–110°E, 20–65°N). All models have smoother topography (e.g., smaller standard deviation) than the ERA-Interim (Fig. S1). The Best5 models have relatively higher spatial standard deviations than other models (Fig. S1). Compared with the Best5 models, the models with a smooth topography substantially underestimate lee cyclogenesis downstream of the mountains. The BCC-CSM-1-1-m, BNU-ESM, and NorESM1-M clearly show such biases (Figs. 4.2c, d, and j).

Figure 4.4 summarizes ETC frequency, intensity, and genesis over East Asia in the ERA-Interim and those in all nine CMIP5 (ALL9) and Best5 models. Note that Figs. 4a and c are identical to Figs. 4.1a and 4.2a, and shown here for the comparison purpose. The East Asian ETCs typically form on the leeward side of mountains and along the Kuroshio-Oyashio extension (Fig. 4.4c), then travel eastward in time (Lee et al. 2020). This makes the most frequent ETCs appear to the east of the Altai-Sayan Mountains and along the Kuroshio-Oyashio extension (Fig. 4.4a). The ETC intensity becomes stronger as the cyclone travels over the ocean (Fig. 4.4b). These features are qualitatively well captured by the CMIP5 models (Figs. 4.4d–f), especially by the Best5 models (Figs. 4.4g–i).

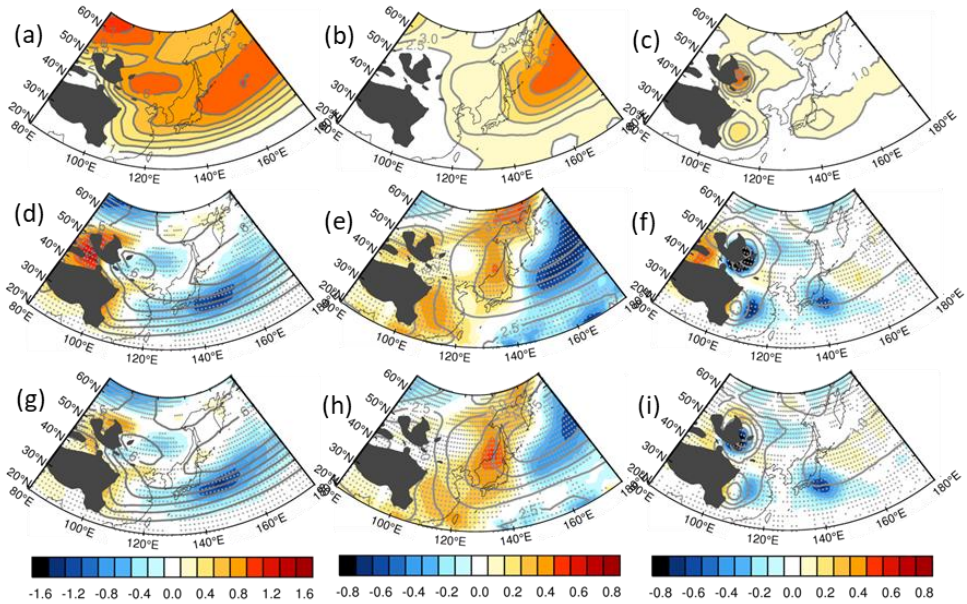

Figure 4.4. (a, b, c) ETC Frequency (# $\mathbf{month^{-1}}$), (d, e, f) intensity (**CVU**), and (g, h, i) genesis (# $\mathbf{month^{-1}}$) over East Asia derived from (top; contours) ERA-Interim, (middle; contours) ALL9, and (bottom; contours) Best5 models for 1979–2004. The differences from ERA-Interim are shaded in (d–i). The gray dots indicate the region where at least 7 models and 4 models have the same sign in ALL9 and Best5 composites. The dark gray mask indicates a 1.5-km high elevation.

The ETC frequency biases in the Best5 models are closely related with the background flow. Figure 4.5a shows that the 300-hPa zonal wind (U300) in the Best5 models is biased poleward with respect to the observation. The positive and negative biases of U300 appear on the poleward and equatorward sides of the climatological U300 center. These biases primarily result from skin temperature biases (Fig. 4.5b) through thermal wind balance. Skin temperature exhibits cold biases over the

continent but warm biases along the Kuroshio current. The net result is an exaggerated meridional temperature gradient on the poleward side of the climatological U300 center but a weak gradient on its equatorward side. These background biases partly explain ETC frequency biases over the ocean south of Japan (Figs. 4.4g and 4.5a). However, their relationship is relatively weak over the East Asian continent and the Kamchatka peninsula.

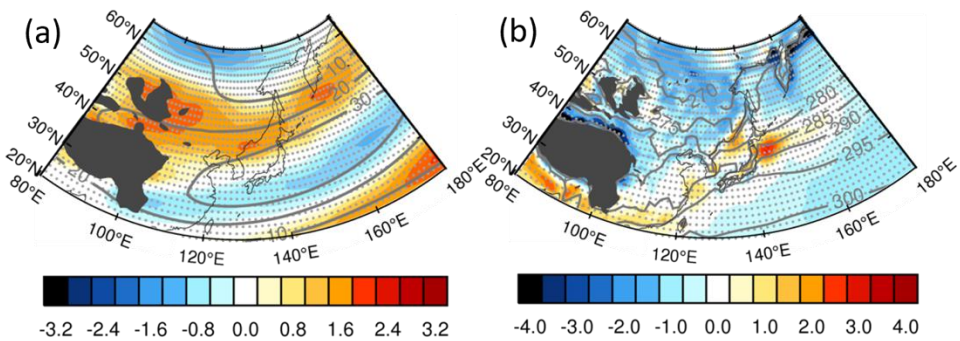

Figure 4.5. (a) Zonal wind at 300 hPa ($\mathrm{m\,s^{-1}}$) and (b) skin temperature (K) in (contours) ERA-Interim for 1979–2004. Shading represents the model bias. The gray dots indicate the region where at least 4 models have the same sign in the Best5 composite. The dark gray mask indicates 1.5-km high elevation.

It is noticeable that the Best5 models still underestimate ETC frequency over the ocean around 35ºN as in the ALL9 models (see blue shadings in Figs. 4.4d and g). This is possibly due to the sea surface temperature gradient which is smoother than the observation. For

instance, sea surface temperature is anomalously warm in East China Sea and east of Japan (Fig. S2), while it is anomalously cold in the North Pacific. This leads to the underestimated temperature gradient resulting in anomalously weak ETC activities.

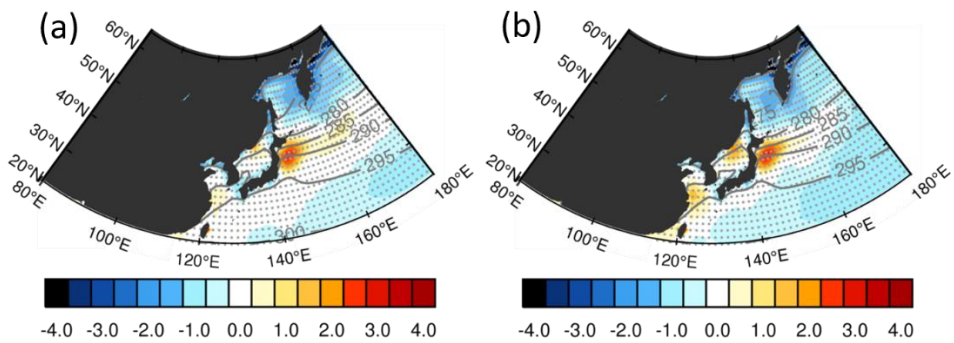

Supplementary figure 2. Sea surface temperature biases in ALL9 and Best5 models from 1979 to 2004. The differences from ERA-Interim are shaded. The gray dots indicate the regions where at least 7 and 4 models agree with the signs of ALL9 and Best5 composites.

The ETC intensity exhibits slightly smaller bias in the Best5 models than ALL9 models near the high-terrain regions, but is still overestimated along the eastern boundary of the Asian continent (Fig. 4.4h), where the land-sea contrast is exaggerated (Fig. 4.5b). These results may suggest that climate models could better represent ETC frequency and intensity by minimizing land temperature and SST biases.

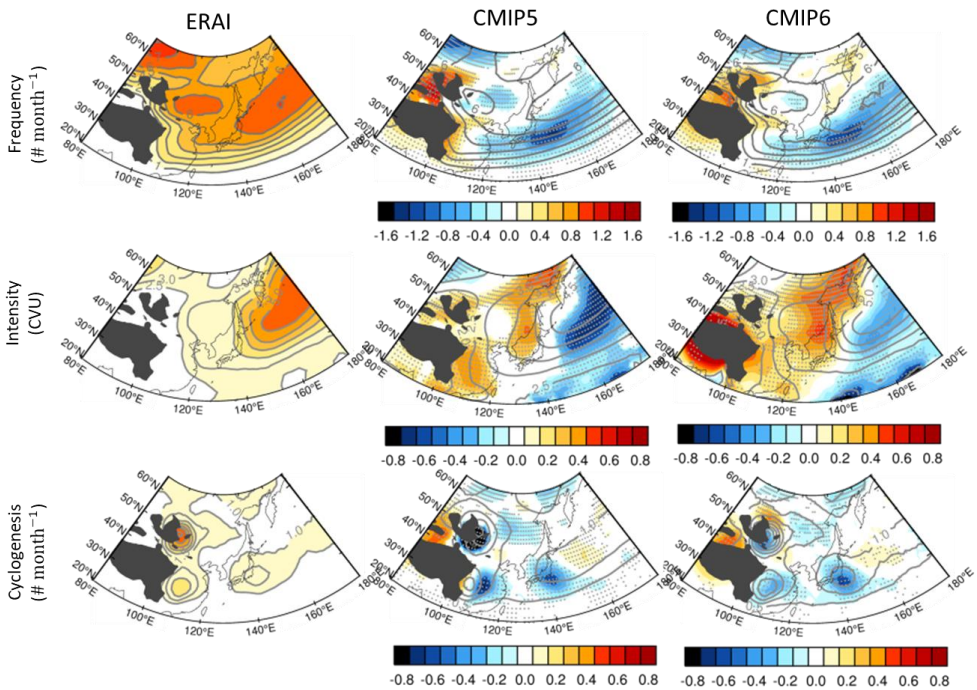

Figure 4.6. (top row) ETC Frequency (# $\mathbf{month^{-1}}$), (middle row) intensity (**CVU**), and (bottom row) genesis (# $\mathbf{month^{-1}}$) over East Asia derived from (left column; contours) ERA-Interim, (middle column; contours) CMIP5, and (right column; contours) CMIP6 models for 1979–2004. The differences from ERA-Interim are shaded in composites of nine CMIP5 and six CMIP6 models. The gray dots indicate the region where at least 7 models and 5 models have the same sign in CMIP5 and CMIP6 composites. The dark gray mask indicates a 1.5-km high elevation.

The robust biases of CMIP5 models are also shown in CMIP6 models. Figure 4.6 exhibits East Asian ETC properties (e.g., ETC frequency, intensity, and cyclogenesis) in ERA-Interim as reference data and the biases of CMIP5 and 6 models. The results of CMIP5 and 6 models are calculated from composites of nine CMIP5 and six CMIP6 models listed in Tables 2.1 and 2.2.

The CMIP6 models have similar spatial patterns of the biases in ETC properties to CMIP5 models: the overestimations of ETC frequency and intensity near mountains and the underestimations of ETC properties downstream of mountains and over the ocean (Fig. 4.6). The ETC frequency and cyclogenesis over the ocean and ETC intensity along the coastlines are biased as much extent in CMIP6 models as in CMIP5 models. But the extents of the biases near mountains of CMIP6 models are lesser than of CMIP5 models–albeit similar spatial distributions. It may be results of fine model resolutions of CMIP6 models but also improved parameterizations regarding the complex interaction between mountains and atmospheric flows.

4.2 Climate change signals of ETC characteristics under RCP 8.5 and SSP5-8.5

The response of East Asian ETCs to increasing greenhouse gas concentrations is examined with the Best5 models (Fig. 4.4). The response is simply defined as the difference between the RCP 8.5 scenario and historical simulations (2074–2099 minus 1979–2004).

The Best5 models project a reduced number of East Asian ETCs with a weakened intensity in a warming climate. The projected ETC frequency and intensity decreases are centered in a narrow band between 25°N and 40°N (Figs. 4.7a and b). The ETC frequency change in this latitude band

is up to 10% of the historical simulations (Fig. 4.7a). The intensity change is larger than the frequency change. The projected ETC intensity is 17% weaker than ETC intensity in the historical simulations (Fig. 4.7b). A reduced ETC frequency is partly due to the reduced cyclogenesis. The cyclogenesis is projected to decrease on the leeward side of the Tibetan Plateau (up to 32% less than historical runs) and over the East China Sea (Fig. 4.7c).

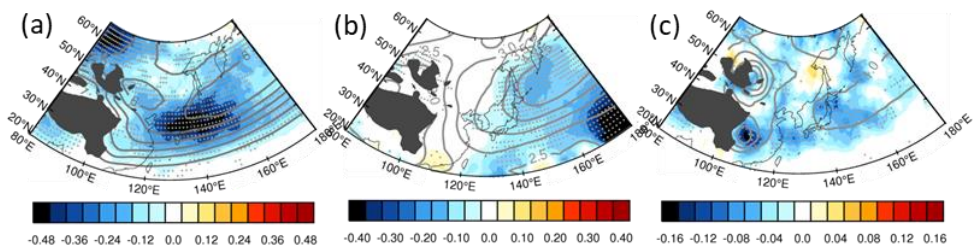

Figure 4.7. (a) ETC Frequency (# $\mathbf{month^{-1}}$), (b) intensity (**CVU**), and (c) genesis (# $\mathbf{month^{-1}}$) over East Asia in the Best5 models for 1979–2004 (contours), and their differences from the RCP 8.5 scenario (2074–2099 minus 1979–2004; shading). The gray dots indicate the region where at least 4 models have the same sign in Best5 composites. The dark gray mask indicates a 1.5-km high elevation.

The projected changes of ETC properties over the East Asian domain (80–180°E, 20–65°N) are further examined for each month in Fig. S3. The reduced and weakened East Asian ETCs in a warming climate are found in all months with a weak seasonality.

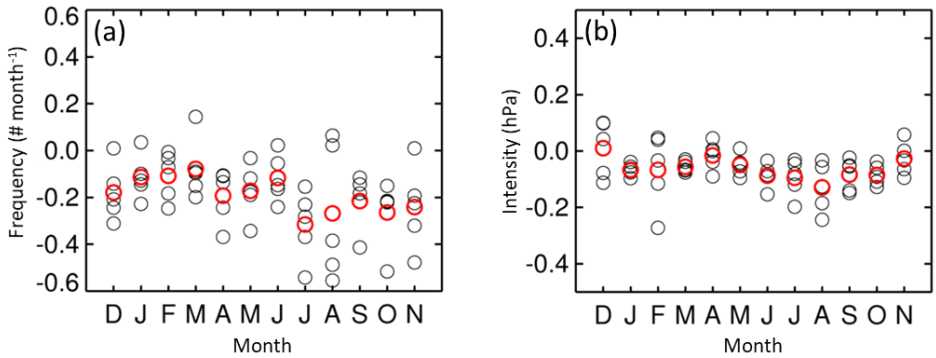

Supplementary figure 3. Future changes of (a) East Asian ETC frequency and (b) intensity month by month. The black circles denote Best5 models (five models), and the red circles represent the Best5 composite. All values are averaged over the East Asian domain (80–180°E, 20–65°N).

Here we emphasize that there is no hint of enhanced ETC activities over East Asia in a warming climate (no red shading in Fig. 4.7). This contrasts with the projected changes of ETC activities over the North Pacific and North Atlantic, where ETC tracks are anticipated to shift poleward (Bengtsson et al. 2006; Ulbrich et al. 2008; Catto et al. 2011). The projected ETC changes in the Best5 models are also robustly found in the ALL9 models, although their magnitudes are smaller (not shown).

Less frequent and relatively weaker ETCs in future climate can be related to the atmospheric background changes. Although the background states are influenced by synoptic weather systems, their changes are more sensitive to the atmospheric thermodynamic changes (e.g., static stability) and surface temperature gradient changes (e.g.,

vertical wind shear) which are externally driven by increasing greenhouse gas concentrations. In this regard, the relationship between the background changes and ETC property changes can provide helpful insight into the future projection of East Asian ETCs. In the present study, Eady growth rate (σ) changes are computed and qualitatively compared with ETC property changes;

$$\sigma = 0.31f|\,\partial u/\partial z\,|N^{-1} \tag{4.5}$$

where f is the Coriolis parameter, u is the zonal wind, and N ($\partial\theta/\partial z$; θ is the potential temperature) is the Brunt-Väisälä frequency. The low-level vertical wind shear and bulk static stability are defined respectively as zonal wind and potential temperature differences between 500 and 850 hPa.

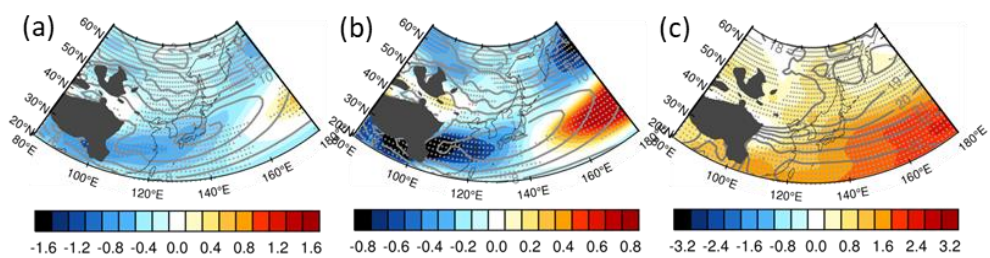

Figure 4.8. (a) Eady growth rate ($\mathbf{day^{-1}}$), (b) low-level vertical wind shear ($\boldsymbol{u_{500} - u_{850}}$; $\mathbf{m\ s^{-1}}$), (c) bulk static stability ($\boldsymbol{\theta_{500} - \theta_{850}}$; $\mathbf{K}$) changes from the historical period to the RCP 8.5 scenarios (2074–2099 minus 1979–2004) in the Best5 models. The gray dots indicate the region where at least 4 models have the same sign in Best5 composites. The dark gray mask indicates 1.5-km high elevation.

Figure 4.8a shows that the Eady growth rate is weakened in the region of reduced ETC frequency (and genesis), implying that less frequent ETCs are closely related with reduced baroclinicity. A weakened baroclinicity from eastern China to the east of Japan well matches with reduced vertical wind shear over the continent (Fig. 4.8b) and enhanced static stability over the ocean (Fig. 4.8c). This wind shear change is mainly determined by the subtropical jet change downstream of the Tibetan Plateau (not shown) which is likely associated with the regional overturning circulation. Staten et al. (2019) reported that the regional overturning circulation is weakened over the Asian continent in future projections. A reduced Eady growth rate also appears in the east of the Kamchatka peninsula (top right in Fig. 4.8a). It is associated with the weakened vertical wind shear in this region (Fig. 4.8b) due to a reduced meridional temperature gradient resulting from an enhanced polar surface warming (not shown). Over the Northwest Pacific Ocean, the vertical wind shear is strengthened but it is largely canceled out by an increased static stability (Figs. 4.8a and c). The net baroclinicity change is positive.

The bulk static stability is enhanced almost everywhere south of 40°N (Fig. 4.8c). This is mostly due to a stronger warming in the mid-troposphere than in the lower troposphere in a warming climate. The

enhancement of the static stability is more remarkable over the northwestern Pacific than over East China, where cyclogenesis is substantially reduced (Fig. 4.7c).

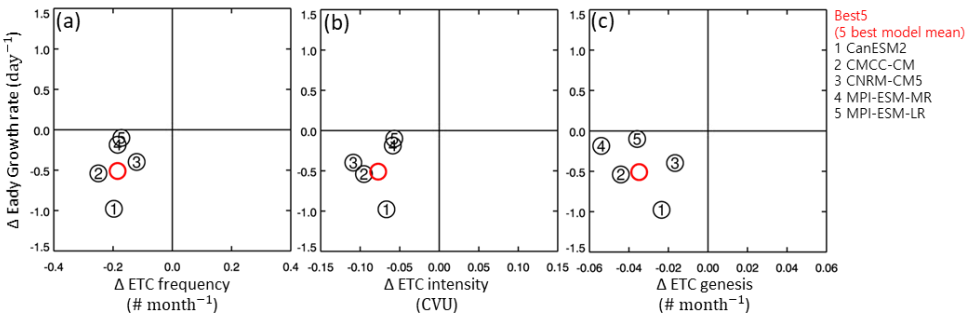

Figure 4.9. Eady growth rate (**day^{-1}**) change versus (a) ETC frequency (# **month^{-1}**) or (b) intensity (**CVU**) or (c) genesis (# **month^{-1}**) change in each Best5 model. All values are averaged over East Asia domain (80–180°E, 20–65°N).

The above result is robustly found in all Best5 models. The inter-model spreads of ETC frequency, intensity, and genesis changes and their relationships to the projected changes of the Eady growth rate are presented in Fig. 4.9. All values shown in this figure are averaged over East Asian domain (80–180°E, 20–65°N). The Best5 models consistently show the reduced ETC frequency (and genesis) and the weakened ETC intensity in a warming climate. It is important to note that all Best5 models show statistically significant ETC property changes at the 95% confidence level based on a two-tailed Student's t-test with the number

of degrees of freedom of 25. The ETC property changes are not linearly related with the baroclinicity changes. For instance, Eady growth rate is substantially reduced in CanESM2 which shows moderate decrease in ETC properties (Fig. 4.9). The CMCC-CM and CNRM-CM5, respectively, show the largest ETC frequency and intensity changes (Figs. 4.9a and b). However, these two models do not show the largest reduction in Eady growth rate. This is likely due to additional factor(s) that affects ETCs. One key factor is the moisture content. It is well known that ETCs are influenced by moisture change (Marciano et al. 2015; Michaelis et al. 2017; Büeler and Pfahl 2019). As the moisture content increases in a warming climate, latent heating associated with ETCs is expected to increase. This could strengthen ETC activities. The relative importance of moisture change against mean flow change, characterized with Eady growth rate, remains to be determined.

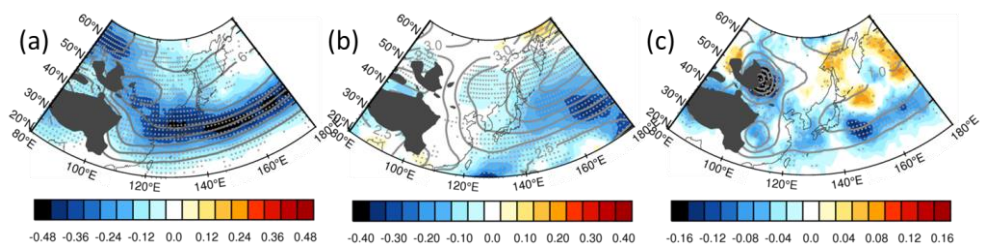

Figure 4.10. Same as Fig. 4.7 but for SSP5-8.5 in CMIP6 models.

The future changes in East Asian ETC properties are reconfirmed in latest models. Figure 4.10 exhibits changes in East Asian ETC properties under SSP5-8.5 scenarios. East Asian ETC frequency is projected to decrease; the decrease of ETC frequency is robust around Korean peninsula and Japan (Fig. 4.10a), matching the results of CMIP5 models. Future changes in ETC intensity–projected by CMIP6 models–are also corresponded to by CMIP5 models; In a warming climate, East Asian ETCs are weakened over the ocean (Fig. 4.10b). But location of mainly decreased cyclogenesis in CMIP6 models is different from in CMIP5 models. The significant reductions of East Asian cyclogenesis is projected in downstream regions of the Tibetan Plateau by CMIP5 models and of the Altai-Sayan mountains by CMIP6 models (Fig. 4.10c). Nevertheless, East Asian cyclogenesis in a warming climate is projected to decrease by CMIP6 models, being similar with the results of CMIP5 models.

4.3 Possible changes of ETC-related precipitation in a warming climate

In previous sections, future change of East Asian ETCs are evaluated using CMIP5 models and the robustness of CMIP5 results is confirmed in CMIP6 models. In both CMIP5 and 6 models, East Asian ETCs are projected to decrease and weaken in a warming climate. A weakened ETC activity has an important implication to regional hydrology as ETC is one

of the important midlatitude systems that determine local precipitation especially in winter (Hawcroft et al. 2012). To evaluate the contributions of future change of East Asian ETCs to East Asian precipitation, we used The European Centre for Medium-range Weather Forecast (ECMWF) Reanalysis 5th Generation (Hersbach et al., 2020; ERA5) and four CMIP6 models which provide 6 hourly precipitations in historical and SSP5-8.5 scenarios: MPI-ESM1-2-HR, MPI-ESM1-2-LR, NorESM2-MM, and NorESM2-LM. Here, we considered only cool season (November to March) which shows the largest contributions of ETCs to precipitation.

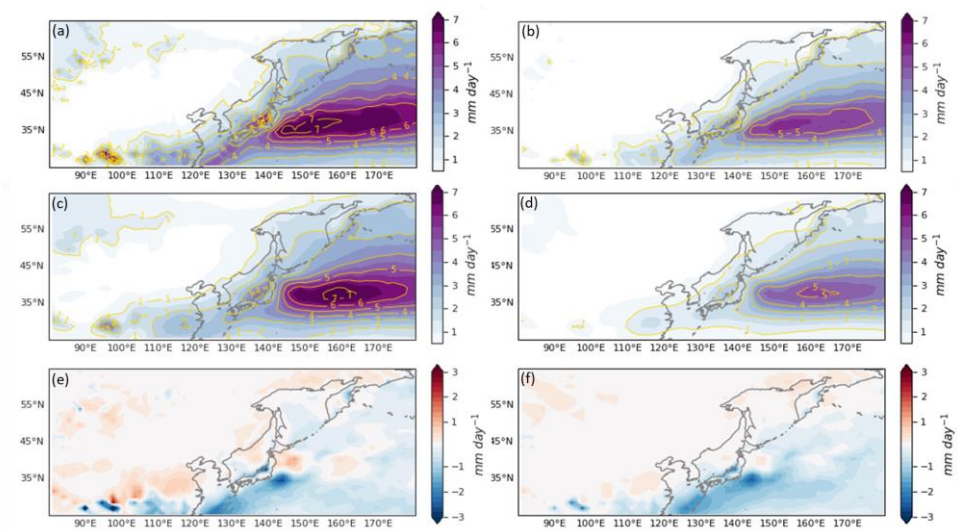

Figure 4.11. (a, c) Total precipitation (**mm day^{-1}**) and (b, d) ETC-related precipitation (**mm day^{-1}**) in the historical period (1979–2004) in (first row) ERA5 and (second row) the CMIP6 composites. The differences between ERA5 and historical runs are shaded in (e, f).

Figure 4.11 shows simulated total and ETC-related precipitations over East Asia in ERA5 and four CMIP6 models. In both CMIP6 historical simulations and ERA5, East Asian total precipitation is the largest (about 7 mm day^{-1}) over the Kuroshio-Oyashio Extension where intense ETCs pass through (Figs. 4.11a and c). In the same region, ETC-related precipitation is also the largest (about 5 mm day^{-1}) and contributes to about 70% of total precipitation (Figs. 4.11a–d). It indicates that East Asian total precipitation in cool seasons is highly contributed by ETC-related precipitation. Figures 4.11e and f exhibits biases of CMIP6 models for total and ETC-related precipitation over East Asia. Overall, CMIP6 models well reproduce the spatial distributions of total and ETC-related precipitations. For instance, historical simulations have maximum total and ETC-related precipitations along the Kuroshio-Oyashio Extension and their local peaks near the west coast of Japan. However, CMIP6 models have some systematic biases. The models underestimate total and ETC-related precipitations over the ocean. These biases are the largest around Japan. These biases are corresponded to strong biases for East Asian ETC frequency and intensity over the ocean. It implies that the underestimated East Asian ETC activity leads to underestimation of total and ETC-related precipitations.

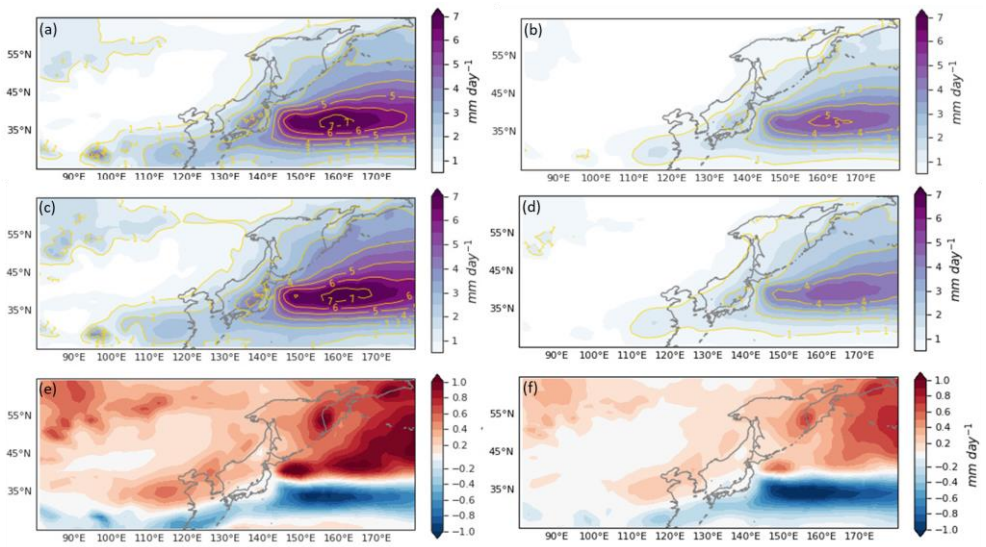

Figure 4.12. Same as Fig. 4.11 but for (first row) historical and (second row) SSP5-8.5 runs.

Based on East Asian total and ETC-related precipitations simulated by CMIP6 models, their possible changes under increasing greenhouse gas forcings are investigated in Fig. 4.12. In a warming climate, total precipitation over East Asia is projected to shift poleward (Fig. 4.12e). The projected increase and decrease of total precipitation are shown in the north and south of maximum total precipitation respectively. The ETC-related precipitation is projected to decrease in the south of the region where the strong reduction of East Asian ETC frequency but is projected to increase in other East Asian regions (Fig. 4.12f). It means that strong weakening of East Asian ETC activity could induce decrease

of ETC-related precipitation despite enhanced moisture content in a warming climate.

As extreme precipitation occurs severe hazards to East Asia, it is very important to understand their possible changes in a warming climate. Figure 4.13 represents the projected changes of extreme total and ETC-related precipitations in a warming climate. Here, extreme precipitation is defined as precipitation over 50 mm day^{-1} following the criterion from World Meteorological Organization Severe Weather Information Centre (https://severeweather.wmo.int/rain/).

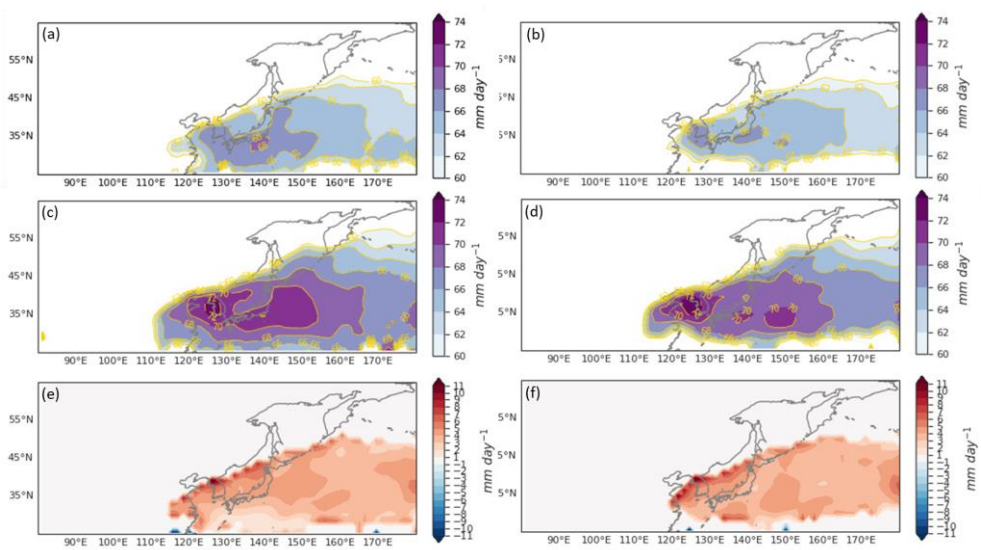

Figure 4.13. Same as Fig. 4.12 but for their extremes.

Extreme total precipitation in historical periods is the largest around Japan and its local intensity is up to 68 mm day $^{-1}$ (Fig. 4.13a). Extreme ETC-related precipitation in historical periods is the largest (up to 66 mm day^{-1}) near the east coast region of East Asia including East Asian populated regions: Korean peninsula and Japan (Fig. 4.13b). The spatial pattern of extreme total precipitation is consistent to that of extreme ETC-related precipitation (Figs. 4.13a and b). It implies that extreme ETC-related precipitation highly contributes to extreme total precipitation. In a warming climate, extreme total and ETC-related precipitations are projected to increase up to 72 mm day^{-1} (Figs. 4.13c and d). Interestingly, total precipitation is projected to increase near the east coast regions of East Asia most strongly: a part of East China and Korean Peninsula (Figs. 4.13c–f). It seems that future change of total precipitation is highly associated with that of ETC-related precipitation.

To examine detailed future change of ETC-related precipitation in East Asia, the joint probability density function with respect to maximum ETC intensity and maximum ETC-related precipitation intensity is analyzed (Fig. 4.14) as ETC intensity is one of the factors that determine ETC-related precipitation intensity.

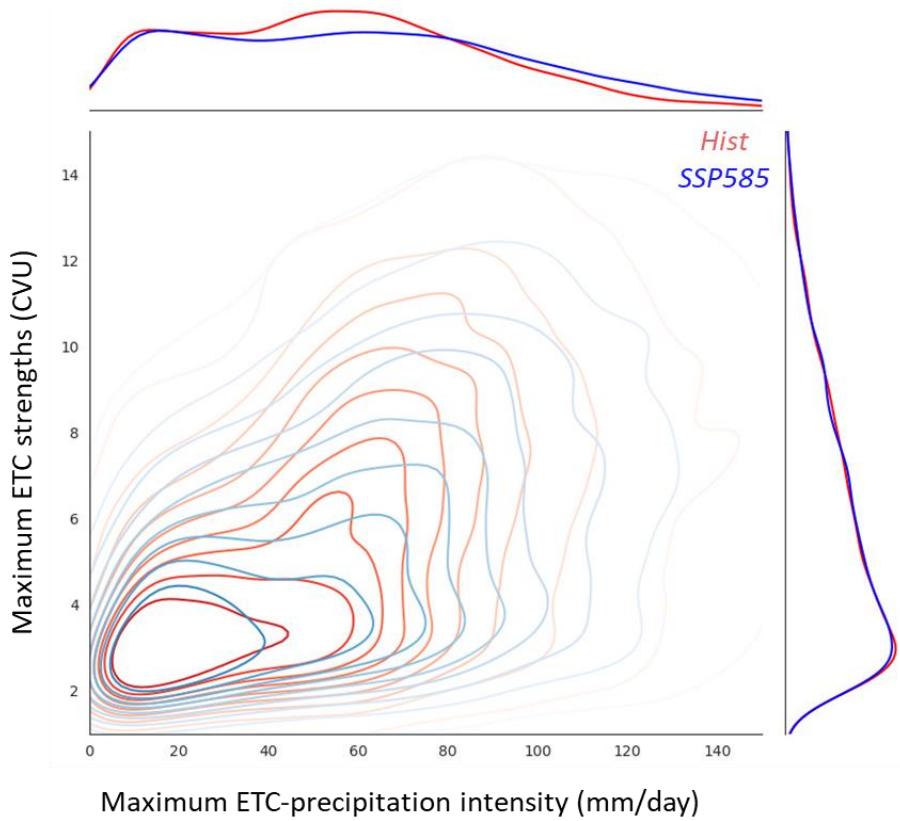

Figure 4.14. The joint probability density functions with respect to maximum ETC intensity (CVU) and ETC-related precipitation intensity (mm day^{-1}) over East Asia. Red and blue lines denote PDFs for historical and SSP5-8.5 runs.

East Asian ETC intensity is projected to slightly decrease in a warming climate. Nevertheless, East Asian ETC-related precipitation shows quite different changes to ETC intensity changes in a warming climate. In East Asia, relatively weak and moderate ETC-related precipitation events (less than 70 mm day^{-1}) are projected to decrease but relatively strong ETC-related precipitation events (over 70 mm day^{-}

[1]) are projected to increase in a warming climate. Extreme ETC-related precipitation's response to a warming climate is contrast to East Asian ETC activity's response. It seems that only weak and moderate ETC-related precipitation is affected by ETC activity, but extremely intense precipitation is affected by other factors rather than ETC activity. It might be associated with increased moisture content. It will be discussed in further study.

Chapter 5. Role of moist and dry processes in extratropical cyclone in the idealized experiment

5.1 Dry simulations

In our dry simulations, water vapor is absent, and all moist processes are not considered. It allows us to see how baroclinicity changes can contribute to ETC intensity changes. This analysis used the minimum surface pressure (SP) at seven days of integration when ETC begins to intensify, as ETC strength rapidly. The results of the dry experiments are used as a baseline test in the moist experiment to examine the role of the moist process in the relationship between baroclinicity and ETC.

5.1.1 Univariate results

The results of DRY_WS and DRY_ST are shown in Fig. 5.1. In DRY_WS, the minimum SP decreases (ETC deepens) as wind shear increases. For every 6 m s^{-1} change in jet amplitude, the minimum SP increases by approximately 0.4 hPa. In DRY_ST, the minimum SP increases as static stability decreases. Even though the minimum SPs do not change much in the strongest static stability conditions (static stability factors of 0.4 and 0.6), most of the minimum SPs increase when static stability

decreases. The results of DRY_WS and DRY_ST are consistent with baroclinic instability theory demonstrated by Eady (1949), who found that the increased horizontal temperature gradient and the weakened stratification make wave amplitude greater (strong ETC) in dry conditions.

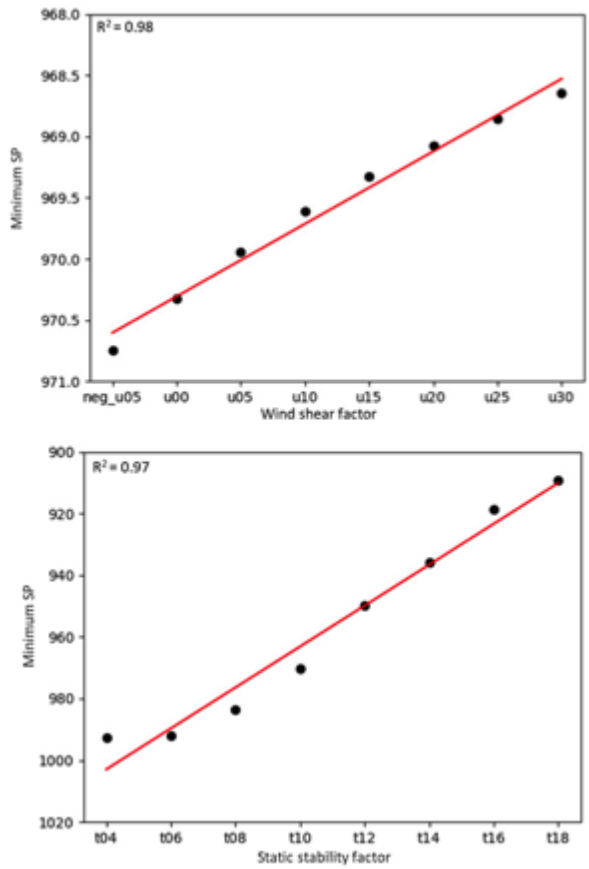

Figure 5.1. The scatterplots for ETC strengths–defined as minimum surface pressure (in hPa)–in univariate sensitivity tests for (top) wind shear and (bottom) static stability. The red line denotes the least squared regression line.

5.1.2 Bivariate sensitivity results

The bivariate test DRY_WS_ST, adjusting both wind shear and static stability simultaneously, consists of 64 runs spanning jet amplitude factors of -0.5~3.0 and static stability factors of 0.4~1.8. This experiment allows us to explore the response of ETCs to possible future changes in wind shear and static stability.

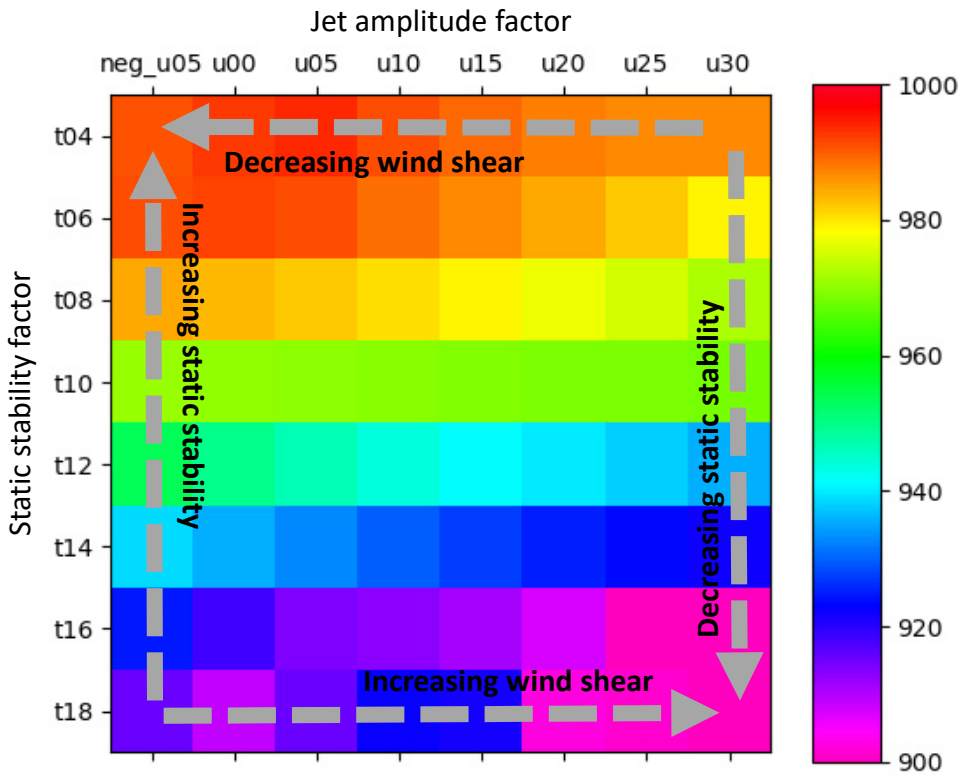

Figure 5.2. Minimum surface pressure (in hPa) at 7 days in bivariate sensitivity test DRY_WS_ST. The surface pressures applied by 9-point local smoothing are used in here.

The bivariate sensitivity test DRY_WS_ST with jet amplitude factors varying on the x-axis and static stability factors varying on the y-axis is shown in Fig. 5.2. Every single box represents the response of ETC intensity defined as minimum SP filtered by 9-point local smoothing. Not surprisingly, most of the responses of ETCs to changes in wind shear and static stability match the results of two univariate tests for two baroclinic components; they have monotonic behavior, even though the non-monotonic response is found in most unstable conditions (lowest static stability; static stability factor of 1.8). For instance, ETC intensity decreases as wind shear decreases and static stability increases. This linear relationship between baroclinicity and ETC strength corresponds to the behavior of ETC in baroclinic unstable and dry conditions demonstrated by Eady (1949). Nevertheless, this can support the result of part 4, which suggested that a decrease in baroclinicity may lead to a decrease in ETC intensity in East Asia. The results of the bivariate sensitivity test in dry conditions are used as a baseline for the bivariate test in moist conditions.

5.2 Moist simulations

In our moist simulation, water vapor and only large-scale condensation is included, allowing us to investigate the effect of latent

heating on the response of ETC in a baroclinic stable or unstable condition. The moist simulation provides the role of the moist process in the development of ETC but also more realistic result than dry simulation. The realistic moist simulation may also hint at the complex interaction between baroclinicity and diabatic heating. In this section, ETC intensity is also represented by the minimum SP of ETC at seven days.

5.2.1 Univariate results

The results of MOI_WS and MOI_ST are shown in Fig. 5.3. The MOI_WS also exhibits ETC deepens monotonically as wind shear increases. For every 6 m s^{-1} change in jet amplitude, the minimum SP increases by approximately 1.5 hPa, which is greater than in DRY_WS. The stronger ETC strength in the moist run than in the dry run is consistent with the results of the previous studies, which showed that the latent heating within ETC can help grow and maintain ETC (Booth et al. 2013; Pfahl et al. 2015). The result of experiment MOI_WS is somewhat consistent with experiment DRY_WS.

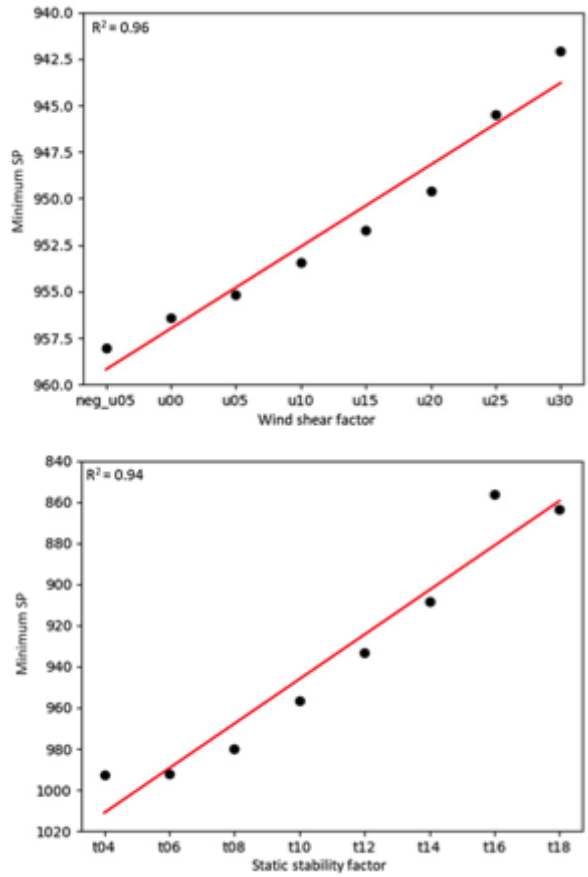

Figure 5.3. Same as Fig. 5.1 but in moist simulation.

The result of experiment MOI_ST is different from experiment DRY_ST. In MOI_ST, the minimum SP response to varying static stability is monotonic in relatively stable conditions (static stability factors of 0.4~1.4), but the response is non-monotonic in relatively unstable conditions (static stability factors of 1.6~1.8). Although baroclinicity changes according to varying static stability in this experiment, this result is consistent with Tierney et al. (2018). They suggested the

nonlinear behavior of ETC response to the change in baroclinicity according to varying wind shear in moist conditions. In short, ETC responds monotonically to varying wind shear with fixed baseline static stability (static stability factor of 1.0) in both dry and moist runs but to varying static stability with fixed baseline wind shear (jet amplitude factor of 0.0) in only dry run.

5.2.2 Bivariate sensitivity results

The structure of the bivariate test MOI_WS_ST, modifying both wind shear and static stability simultaneously, is the same as that of DRY_WS_ST, which is a series of 64 runs adjusting wind shear (jet amplitude factors of -0.5~3.0) and static stability (static stability factors of 0.4~1.8) but includes moisture content and considers large scale condensation related to latent heating within ETC. This moist experiment allows us to investigate the sensitivity of ETCs to changes in baroclinicity in moist conditions.

The result of MOI_WS_ST is shown in Fig. 5.4. The bivariate sensitivity test MOI_WS_ST is consistent with univariate sensitivity tests MOI_WS and MOI_ST in baroclinically stable conditions. In relatively stable stability conditions (static stability factors of 0.4~1.0), the ETC grows strongly as wind shear increases; in relatively weak wind shear

conditions (jet amplitude factors of -0.5~1.5), the ETC intensifies highly as static stability decreases. This result of the realistic moist run indicates that a decrease in baroclinicity can weaken ETCs even in moist conditions, supporting the causality of future changes in baroclinicity and ETC intensity in CMIP5 models in part 4.

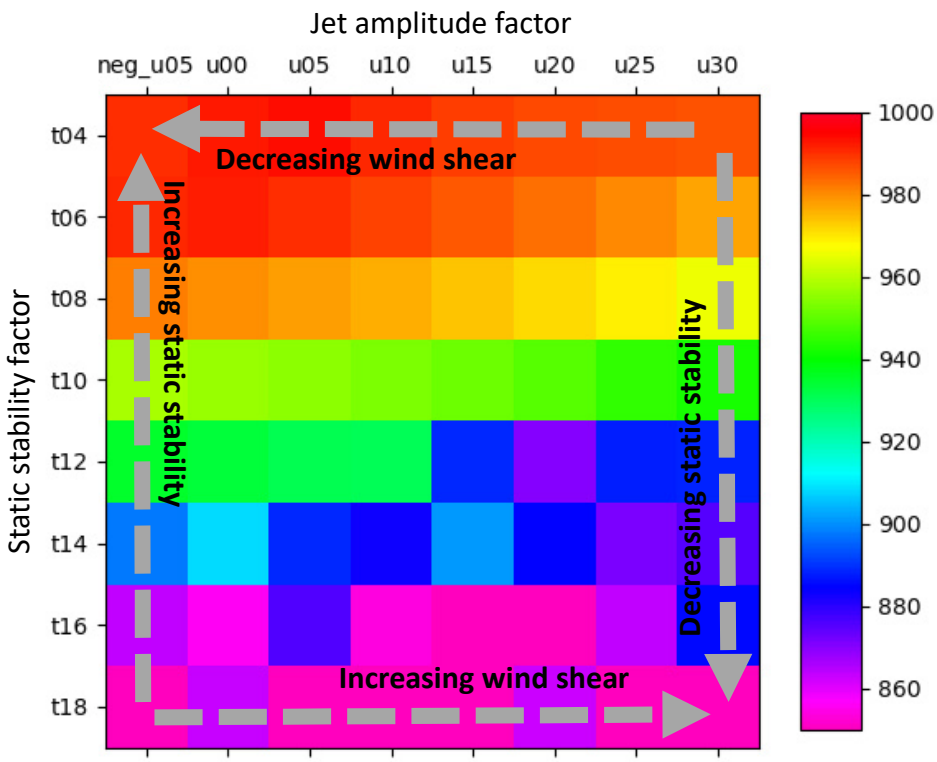

Figure 5.4. Same as Fig. 5. but in moist run.

In addition, it is confirmed that ETC does not respond monotonically to changes in two baroclinic components in highly baroclinically unstable conditions. In strongly unstable stability conditions (static stability factors of 1.2~1.8), ETC strength does not linearly respond to change in wind shear; in greatly strong wind shear conditions (jet amplitude factors of 2.0~3.0), ETC intensity does not linearly respond to in static stability. For instance, ETC intensity (approximately 890 hPa) in relatively strong baroclinicity condition (jet amplitude factor of 2.0 and static stability factor of 1.4) is larger than that (approximately 870 hPa) in relatively weak baroclinicity condition (jet amplitude factor of 2.0 and static stability factor of 1.2). This non-monotonic ETC response corresponds to Tierney et al. (2018), who manipulated only wind shear for modifying baroclinicity, indicating that the moist process may occur non-monotonic ETC response to change in baroclinicity under highly unstable baroclinic conditions.

Chapter 6. Summary and discussion

This study aims to understand climatic features of East Asian ETCs; then explore the responses of East Asian ETCs to climate change; understand East Asian ETC response to changing climate. In first part, ETC climatology, seasonality, and their long-term trends over East Asia are examined. The second part evaluates the simulated ETCs in CMIP5 and 6 models and the possible change of ETCs in a warming climate. The third part examines the causality of changes in baroclinicity and ETCs in changing climate and the role of moist process in this relationship.

The study in first part documents the climatological properties of East Asian ETCs that are detected and tracked with an automated tracking algorithm applied to an 850-hPa relative vorticity field. East Asian ETCs exhibit three regions of maximum cyclogenesis (i.e., Mongolia, South China, and the Kuroshio Current region). Developing cyclones typically form in the downstream region of mountains (e.g., Mongolia and South China ETCs) and over the Kuroshio region (Kuroshio ETCs). While the former ETCs are generated by lee cyclogenesis, the latter ETCs are organized by baroclinic instability and diabatic processes. These cyclones commonly strengthen with time but have somewhat different seasonality for their genesis regions. Both Mongolia and South China ETCs show a maximum frequency and intensity in spring rather than in

winter. While Mongolia ETCs are also frequent in fall, South China ETCs are not well defined in fall. This implies that development mechanisms of these two ETCs may differ with seasons (Kang et al. 2020). The Kuroshio ETCs also exhibit a maximum intensity in spring, but their frequency is maximum in winter.

Most ETCs rapidly grow over the Kuroshio–Oyashio extension as they travel eastward or northeastward, then decay over the Okhotsk Sea. Both growth and decay rates are maximum in winter but minimum in summer. In winter, ETCs have a relatively short lifetime and move fast over a long distance. Compared with them, summer ETCs are maintained longer and move slower because of weak background flow.

In term of the long-term trend, East Asian ETCs show a hint of the decreasing trend in their frequency. The significant trends appear at different seasons and regions. Only continental ETCs exhibit statistically significant trends in two seasons. The number of Mongolia ETCs has significantly decreased in summer, while South China ETCs has significantly reduced in spring. This result indicates that the two continental ETCs (i.e., Mongolia and South China ETCs) have different long-term variability. Although the detailed dynamic mechanisms remain

to be determined, these trends are at least consistent with enhanced static stability which is caused by global warming.

On the view of the impacts of those two ETCs on East Asian weather, these trends might give a hint of the occurrences of various ETC-related weather events in future. For instance, rapidly developing Mongolia ETCs pass through the source region of East Asian dust, and they often occur East Asian dust events. Due to Mongolia ETCs' weather impact, decreasing Mongolia ETCs trend could imply the decrease of East Asian dust events in future. South China ETCs are also closely related to East Asian precipitation. The previous study (Kim et al. 2021) have already mentioned that South China ETCs developing by the strong diabatic heating transport a huge amount of moisture to East Asia, and they are closely associated with East Asian precipitation.

To better understand East Asian ETC properties, an extended study is needed. Among others, intraseasonal and interannual variabilities need to be addressed (e.g., Grise et al. 2013). A preliminary analysis of the year-to-year variability of wintertime ETCs shows that East Asian ETCs are more active during El Niño winters than during La Niña winters. This is particularly true for South China ETC frequency. The El Niño-related ETC activities are also pronounced in the south of Japan. As

discussed in Ueda et al. (2017), ETC frequency in this region significantly increases during El Niño winters because of a weakened subtropical jet. Note that a strong subtropical jet tends to suppress cyclogenesis in this region (Nakamura and Sampe 2002).

In second part, the model biases and future projections of East Asian ETCs are analyzed with nine CMIP5 models which provide 6-hourly data with no missing values over the Tibetan Plateau. Most models qualitatively capture the spatial distribution of East Asian ETCs, although systematic biases are still found in the vicinity of the high terrain regions and over the western North Pacific. The ETC frequency and genesis are underestimated downstream of the mountains and over the Kuroshio-Oyashio extension. While ETC intensity is overestimated over the continent, it is underestimated over the western North Pacific.

Although there is uncertainty in magnitude of future changes, the five best models (CMCC-CM, CNRM-CM5, CanESM2, MPI-ESM-MR, and MPI-ESM-LR; Best5 models) with a relatively high spatial resolution and topography show that East Asian ETC frequency and intensity are projected to decrease in a warming climate. These changes are robustly found across all seasons (Fig. S3). The ETC frequency change is closely related to the reduced cyclogenesis over the region which is partly

explained by the projected decrease in local baroclinicity. A weakened subtropical jet over the continent and an enhanced static stability over the ocean below 40°N act to weak local baroclinicity.

Here, it is important to state that ETC changes reported in this study should be understood only in quality. Although the Best5 models show systematic reductions in East Asian ETC frequency and intensity in a warming climate, their changes are comparable to the model biases. More models with higher resolution would be required to obtain robust results. This is particularly true for quantifying ETC-related precipitation changes.

The present study is mainly based on the CMIP5 dataset, extending this study to the latest models. The CMIP6 models show qualitatively similar results with negative trends of ETC properties in a warming climate. The similarity and contrast of the CMIP6 models to the CMIP5 models support the results in CMIP5 models.

Based on consistent future changes of East Asian ETCs in both CMIP5 and 6 models, future change of precipitation related to ETCs in cool seasons, which have strong relationship between ETCs and precipitation, is investigated using four CMIP6 models providing 6-hourly precipitation data. The ETC-related precipitation is projected to

decrease near the region where the largest decrease of East Asian ETC activity is projected; this decrease is reduced total precipitation in a warming climate. Nevertheless, extreme ETC-related precipitation is projected to increase in a warming climate. It means that East Asian ETC changes in a warming climate could lead to change of relatively weak and moderate ETC-related precipitation; but it doesn't seem to affect relatively strong ETC-related precipitation. It will be studied in further study.

In third part, the idealized model experiments are conducted to understand the impact of change in background states under climate change on ETC. In the idealized experiments, changes in two baroclinic components in future climate are considered: change in wind shear (due to varying jet amplitude) and static stability (due to adjusting potential temperature profile). The effects of those two factors on ETC are isolated in each univariate test. In addition, the ETC response to simultaneous changes in two baroclinic components is investigated in the bivariate sensitivity test. The experiments are performed in dry and moist conditions to examine the role of the moist process in ETC response to change in baroclinicity under future climate scenarios.

An increase in wind shear results in more intense ETC in both dry and moist runs, following the traditional baroclinic instability theory demonstrated by Eady (1949). Furthermore, the extent to which ETC strength increases due to enhanced baroclinicity is larger in moist runs than in dry runs. These results are consistent with Booth et al. (2013), Pfahl et al. (2015), and Tierney et al. (2019), who adjusted baroclinicity by manipulating jet amplitude.

A decrease in static stability turned out stronger ETC in dry simulation. The ETC response to static stability in the moist simulation is more complicated than in the dry simulation. In the highest unstable stability condition, ETC does not grow monotonically as static stability decreases. It may be due to a change in static stability due to an increase in latent heating within ETC, as already suggested by O'gorman (2011), who introduced that the latent heat release at mid-troposphere could increase static stability at the lower troposphere. It needs to examine how latent heating within ETC affects static stability under various initial static stability conditions.

Based on the univariate tests, the bivariate sensitivity test varying two factors simultaneously is conducted for a more comprehensive investigation of background states in future climate. This bivariate test

allows us to consider the interaction between two baroclinic factors. Naturally, the result of the bivariate test in the dry run matches both univariate tests, corresponding to baroclinic instability theory. For instance, ETC strength decreases as wind shear decreases and static stability increases. It implies that if the impact of the moist process on the growth of ETC is not as much as that of baroclinicity, the change in ETC intensity depends on baroclinicity.

The bivariate test in moist run exhibits a more complex response of ETC to changes in two baroclinic components. In an environment with relatively weak baroclinicity, ETC strength in a moist run monotonically responds to changes in wind shear and static stability even with a moist process, coinciding with a dry run. It implies that if baroclinicity in changing climate is not relatively stronger than at present, change in ETC intensity depends on baroclinicity. However, the ETC strength shows a different response in a relatively strong baroclinicity environment. In this environment, ETC strength does not depend on baroclinicity. It is revealed that ETC strength in stronger baroclinicity (higher wind shear and lower static stability) conditions is lower than in weaker baroclinicity. These results indicate that the nonlinear ETC response to the change in baroclinicity in a moist condition caused by the complex interaction between latent heating and baroclinicity demonstrated by

O'gorman (2011) is only applicable to sufficiently intense ETCs with the strong initial baroclinicity.

References

Adachi, S., and F. Kimura, 2007: A 36-year climatology of surface cyclogenesis in East Asia using high-resolution reanalysis data. *SOLA*, **3 ,** 113–116.

Ahn, J. B., J.-H. Ryu, E.-H. Cho, J.-Y. Park, S.-B. Ryoo, 1997: A Study on correlation between air-temperature and precipitation in Korea and SST over the Tropical Pacific (in Korean). *J. Korean Meteorol. Soc.*, **33**, 487–495.

Beljaars, A., A. Brown, and N. Wood, 2004: A new parameterization of turbulent orographic form drag, *Quart. J. Roy. Meteor. Soc.*, **130**, 1327–1347.

Bengtsson, L., K. I. Hodges, and E. Roeckner, 2006: Storm tracks and climate change. *J. Climate*, **19 ,** 3518–3543.

——, ——, and N. Keenlyside, 2009: Will extratropical storms intensify in a warmer climate?. *J. Climate*, **22(9)**, 2276-2301.

Blackmon, M. L., J. M. Wallace, N.-C. Lau, and S. L. Mullen, 1977:An observational study of the Northern Hemisphere wintertime circulation. *J. Atmos. Sci.,* **34,** 1040–1053.

Blender, R., K. Fraedrich, and F. Lunkeit, 1997: Identification of cyclone track regimes in the North Atlantic. *Quart. J. Roy. Meteor. Soc.*,**123**, 727–741.

——, and M. Schubert, 2000: Cyclone tracking in different spatial and temporal resolutions. *Mon. Wea . Rev.*, **128**, 377–384.

Booth, J. F., S. Wang, and L. M. Polvani, 2013: Midlatitude storms in a moister world: lessons from idealized baroclinic life cycle experiments. *Clim. Dyn.*, **41**, 787–802

Catto, J. L., L. C. Shaffrey, and K. I. Hodges, 2011: Northern Hemisphere

extratropical cyclones in a warming climate in the HiGEM high-resolution climate model. *J. Climate*, **24(20)**, 5336-5352.

Catto, J. L., and Coauthors, 2019: The future of midlatitude cyclones. *Curr. Climate Change Rep.*, **5**, 407–420.

Chang, E. K. M., Y. Guo, and X. Xia, 2012: CMIP5 multimodel ensemble projection of storm track change under global warming. *J. Geophys. Res. Atmos.*, **117(D23)**.

Chang, E. K. M., S. Lee, and K. L. Swanson, 2002: Storm track dynamics. *J. Climate*, **15 ,** 2163–2183.

Charney, J. G., 1947: The dynamics of long waves in a baroclinic westerly current. *J. Meteor.*, **4**, 135–63.

Chen, S.-J., and L. Lazic, 1990: Numerical case study of the Altai-Sayan lee cyclogenesis over east Asia. *Meteor. Atmos. Phys.,***42,** 221–229.

——, Y-H. Kuo, P-Z. Zhang, and Q-F. Bai, 1991: Synoptic climatology of cyclogenesis over East Asia, 1958–1987. *Mon. Wea. Rev.*, **119 ,** 1407–1418.

——, ——, ——, and ——, 1992: Climatology of explosive cyclones off the east Asian coast. *Mon. Wea. Rev.*, **120 ,** 3029–3035.

——, and P. Z. Zhang, 1996: Climatology of deep cyclones over Asia and the Northwest Pacific. *Theor. Appl. Climatol.*, **54**, 139–146.

Chen, X., Y. Liu, and G. Wu, 2017: Understanding the surface temperature cold bias in CMIP5 AGCMs over the Tibetan Plateau. *Adv. Atmos. Sci.*, **34**, 1447–1460.

Chen, L., B. K. Tan, N. G. Kvamstø, and O. M. Johannessen, 2014: Wintertime cyclone/anticyclone activity over China and its relation to upper tropospheric jets. *Tellus A*, **66**, 21889.

Cho, H.-O., S.-W. Son, and D.-S. Park, 2018: Springtime extra-tropical cyclones in Northeast Asia and their impacts on long-term

precipitation trends. *Int. J. Climatol.*, **38**, 4043–4050.

Chung, Y-S., K. D. Hage, and E. R. Reinelt, 1976: On lee cyclogenesis and airflow in the Canadian Rocky Mountains and the East Asian mountains. *Mon. Wea. Rev.*, **104 ,** 879–891.

Collins, M., and Coauthors, 2014: Long-term climate change: Projections, commitments and irreversibility. *Climate Change 2013: The Physical Science Basis,* T. F. Stocker et al., Eds., Cambridge University Press, 1029–1136.

Colle, B. A., Z. Zhang, K. A. Lombardo, and E. Chang, P. Liu, and M. Zhang, 2013: Historical evaluation and future prediction of eastern North American and western Atlantic extratropical cyclones in the CMIP5 models during the cool season. *J. Climate*, **26(18)**, 6882-6903.

Côté, H., K. M. Grise, S.-W. Son, R. de Elía, and A. Frigon, 2015: Challenges of tracking extratropical cyclones in regional climate models. *Climate Dyn.*, **44**, 3101–3109.

Dee, D., and Coauthors, 2011: The ERA-Interim reanalysis: Configuration and performance of the data assimilation system. *Quart. J. Roy. Meteor. Soc.*, **137**, 553–597.

Della-Marta, P. M., and J. G. Pinto, 2009: Statistical uncertainty of changes in winter storms over the North Atlantic and Europe in an ensemble of transient climate simulations. *Geophys. Res. Lett.*, **36**, L14703.

Eady, E. T., 1949: Long waves and cyclone waves. *Tellus*, **1 ,** 33–52.

Eichler, T. P., N. Gaggini, and Z. Pan, 2013: Impacts of global warming on Northern Hemisphere winter storm tracks in the CMIP5 model suite. *J. Geophys. Res. Atmos.*, **118**, 3919–3932.

——, and W. Higgins, 2006: Climatology and ENSO-related variability of North American extratropical cyclone activity. *J. Climate*, **19 ,** 2076–2093.

Eyring, V., S. Bony, G. A. Meehl, C. Senior, B. Stevens, R. J. Stouffer, and K. E. Taylor, 2016: Overview of the Coupled Model Intercomparison Project Phase 6 (CMIP6) experimental design and organization. *Geosci. Model Dev.*, **9**, 1937–1958.

Fink, A. H., T. Brücher, V. Ermert, A. Krüger, and J. G. Pinto, 2009: The European storm Kyrill in January 2007: synoptic evolution, meteorological impacts and some considerations with respect to climate change. *Nat. Hazards Earth Syst. Sci.*, **9(2)**, 405-423.

Gill, A. E., 1980: Some simple solutions for heat-induced tropical circulation. *Quart. J. Roy. Meteor. Soc.,* **106,** 447–462.

Graham, N. E., and H. F. Diaz, 2001: Evidence for intensification of North Pacific winter cyclones since 1948. *Bull. Amer. Meteor. Soc.*, **82 ,** 1869–1893.

Grise, K. M., S.-W. Son, and J. R. Gyakum, 2013: Intraseasonal and interannual variability in North American storm tracks and its relationship to equatorial Pacific variability. *Mon. Wea. Rev.*, **141**, 3610–3625.

Hersbach, H., B. Bell, P. Berrisford, S. Hirahara, A. Horányi, J. Muñoz-Sabater, and J. N. Thépaut, 2020: The ERA5 global reanalysis. *Quart. J. Roy. Meteor. Soc.*, **146**, 1999–2049.

Hartmann, D. L., 1994: *Global Physical Climatology*. Academic Press.

Hawcroft, M. K., L. C. Shaffrey, and H. F. Dacre, 2012: How much Northern Hemisphere precipitation is associated with extratropical cyclones? *Geophys. Res. Lett.*, **39**, L24809.

Hayasaki, M., R. Kawamura, M. Mori, and M. Watanabe, 2013: Response of extratropical cyclone activity to the Kuroshio large meander in northern winter. *Geophys. Res. Lett.*, **40**, 2851–2855.

Held, I. and B. Soden, 2006: Robust responses of the hydrological cycle to

global warming. *J. Clim.*, **19**, 5686–5699.

Heo, K. Y., K. J. Ha, and T. Ha, 2019: Explosive cyclogenesis around the Korean Peninsula in May 2016 from a potential vorticity perspective: Case study and numerical simulations. *Atmosphere*, **10**(6), 322.

——, Y.-W. Seo, K.-J. Ha, K.-S. Park, J. Kima, J.-W. Choia, K. Juna, and J.-Y. Jeonga, 2015: Development mechanisms of an explosive cyclone over East Sea on 3–4 April 2012. *Dyn. Atmos. Oceans*, **70**, 30–46.

Hersbach, H., and Coauthors, 2020: The ERA5 global reanalysis. *Quart. J. Roy. Meteor. Soc.*, **146**, 1999–2049.

Hirata, H., R. Kawamura, M. Kato, and T. Shinoda, 2015: Influential role of moisture supply from the Kuroshio/Kuroshio Extension in the rapid development of an extratropical cyclone. *Mon. Wea. Rev.*, **143**, 4126–4144.

Hodges, K. I., 1994: A general method for tracking analysis and its application to meteorological data. *Mon. Wea. Rev.*, **122 ,** 2573–2586.

——, 1995: Feature tracking on the unit sphere. *Mon. Wea. Rev.*, **123**, 3458–3465.

——, 1999: Adaptive constraints for feature tracking. *Mon. Wea. Rev.*, **127 ,** 1362–1373.

Hong, S.-Y., and Coauthors, 2013: The Global/Regional Integrated Model System (GRIMs). *Asia-Pac. J. Atmos. Sci.*, **49**, 219–243.

Hoskins, B. J., M. E. McIntyre, and A. W. Robertson, 1985: On the use and significance of isentropic potential vorticity maps. *Quart. J. Roy. Meteor. Soc.*, **111 ,** 877–946.

——, and K. I. Hodges, 2002: New perspectives on the Northern Hemisphere winter storm tracks. *J. Atmos. Sci.*, **59 ,** 1041–1061.

Huffman, G. J.,R. F. Adler, M. M. Morrissey, S. Curtis, R. Joyce, B. McGavock, and J. Susskind, 2001: Global precipitation at one-degree daily

resolution from multi-satellite observations. *J. Hydrometeor.*, **2**, 36-50.

Inatsu, M., 2009: The neighbor enclosed area tracking algorithm for extratropical wintertime cyclones. *Atmos. Sci. Lett.*, **10**, 267–272.

IPCC (2014) Climate change 2014: synthesis report. In: Pachauri, R. K., L. A. Meyer (eds) Contribution of working groups I, II and III to the Fifth Assessment Report of the Intergovernmental Panel on Climate Change [Core Writing Team]. IPCC, Geneva.

Iwao, K., M. Inatsu, and M. Kimoto, 2012: Recent changes in explosively developing extratropical cyclones over the winter northwestern Pacific. *J. Climate*, **25**, 7282–7296.

Jablonowski, C., and D. L. Williamson, 2006: A baroclinic wave test case for dynamical cores of general circulation models: Model intercomparisons. NCAR Tech. Note NCAR/TN-469+STR, 75 pp.

Jung, M.-I., S.-W. Son, H.-C. Kim, S.-W. Kim, and R. J. Park, 2019: Contrasting synoptic weather patterns between non-dust high particulate matter events and Asian dust events in Seoul, South Korea. *Atmos. Environ.*, **214**, 116864.

Kang, J. M., J. Lee, S.-W. Son, J. Kim, and D. Chen, 2020: The rapid intensification of East Asian cyclones around the Korean Peninsula and their surface impacts. *J. Geophys. Res. Atmos.*, **125**, e2019JD031632.

Kim, D., J. Lee, J. M. Kang, and S. W. Son, 2021: Synoptic Structures and Precipitation Impact of Extratropical Cyclones Influencing on East Asia Megacities: Seoul, Beijing, Tokyo (in Korean). *Atmosphere*, **31(1)**, 45-60.

Kim, S., and J.-S. Kug, 2018: What controls ENSO teleconnection to East Asia? Role of western North Pacific precipitation in ENSO teleconnection to East Asia. *J. Geophys. Res. Atmos.*, **123**, 10 406–410,

422.

Kirshbaum, D. J., T. M. Merlis, J. R. Gyakum, and R. McTaggart-Cowan, 2018: Sensitivity of idealized moist baroclinic waves to environmental temperature and moisture content. *J. Atmos. Sci.*, **75**, 337–360.

Kuo, Y. H., M. A. Shapiro, and E. G. Donall, 1991: The interaction between baroclinic and diabatic processes in a numerical simulation of a rapidly intensifying extratropical marine cyclone. *Mon. Wea. Rev.*, **119(2)**, 368-384.

Lambert, S. J., 1996: Intense extratropical northern hemisphere winter cyclone events: 1899–1991. *J. Geophy. Res.*, **101 ,** 21 319–21 325.

——, and J. C. Fyfe, 2006: Changes in winter cyclone frequencies and strengths simulated in enhanced greenhouse warming experiments: Results from the models participating in the IPCC diagnostic exercise. *Climate Dyn.*, **26 ,** 713–728.

Lamb, H., and K. Frydendahl, 1991: *Historic Storms of the North Sea, British Isles and Northwest Europe*. Cambridge University Press.

Leckebusch, G. C., and U. Ulbrich, 2004: On the relationship between cyclones and extreme windstorm events over Europe under climate change. *Global Planet. Change*, **44**, 181–193.

Lee, D.-K., C.-H. Joung, S.-U. Park, S.-C. Yoon, C.-W. Lee, Y.-H. Kuo, and S. Low-Nam, 1991: Numerical simulations of an explosive cyclogenesis near the East Asian coast (in Korean). *Atmosphere*, **27**, 1–21.

Lee, H.-R., K.-E. Kim, J.-H. Park, and B. Campisitron, 2009: Eulerian characteristics of the meteorological fields of an explosive cyclone linked to a tropopause fold. *Asia-Pacific J. Atmos. Sci.*, **45**(4), 555–573.

Lee, J., J. Kim, and S.-W. Son, 2016: Climatic features of extratropical

cyclones during the spring-time yellow dust events in Korea (in Korean). *Atmosphere*, **26**, 565–576.

——, S.-W. Son, H.-O. Cho, J. Kim, D.-H. Cha, J. R. Gyakum, and D. Chen, 2020: Extratropical cyclones over East Asia: Climatology, seasonal cycle, and long-term trend. *Climate Dyn.*, **54**, 1131–1144.

Lott, F., and M. Miller, 1997: A new subgrid orographic drag parameterization: Its formulation and testing, *Quart. J. Roy. Meteor. Soc.*, **123**, 101–127.

Löptien, U., O. Zolina, S. Gulev, M. Latif, and V. Soloviov, 2008: Cyclone life cycle characteristics over the Northern Hemisphere in coupled GCMs. *Climate Dyn.*, **31 ,** 507–532.

Madonna, E., H. Wernli, H. Joos, and O. Martius, 2014: Warm conveyor belts in the ERA-Interim dataset (1979–2010). Part I: Climatology and potential vorticity evolution. *J. Climate,* **27,** 3–26.

Marciano, C. G., G. M. Lackmann, and W. A. Robinson, 2015: Changes in U.S. east coast cyclone dynamics with climate change. *J. Climate*, **28**, 468–484.

Michaelis, A. C., J. Willison, G. M. Lackmann, and W. A. Robinson, 2017: Changes in winter North Atlantic extratropical cyclones in high-resolution regional pseudo–global warming simulations. *J. Climate*, **30**, 6905–6925.

Muskulus, M., and D. Jacob, 2005: Tracking cyclones in regional model data: The future of Mediterranean storms. *Adv. Geosci.*, **2 ,** 13–19.

Nakamura, H., 1992: Midwinter suppression of baroclinic wave activity in the Pacific. *J. Atmos. Sci.*, **49 ,** 1629–1642.

——, and T. Sampe, 2002: Trapping of synoptic-scale disturbances into the North Pacific subtropical jet core. *Geophys. Res. Lett.,* **29,** 1761.

Neu, U., and Coauthors, 2012: IMILAST—A community effort to

intercompare extratropical cyclone detection and tracking algorithms: Assessing method-related uncertainties. *Bull. Amer. Meteor. Soc.*, **94,** 529–547.

O'Gorman, P. A., 2011: The effective static stability experienced by eddies in a moist atmosphere. *J. Atmos. Sci.*, **68**, 75–90.

Park, C., S.-W. Son, H. Kim, Y.-G. Ham, J. Kim, D.-H. Cha, E.-C. Chang, G. Lee, J.-S. Kug, W.-S. Lee, Y.-Y. Lee, H. C. Lee, and B. Lim, 2021: Record-breaking summer rainfall in South Korea in 2020: Synoptic characteristics and the role of large-scale circulations. *Mon. Wea. Rev*.

Petterssen, S., 1956: *Weather Analysis and Forecasting*. Vol. 1. McGraw-Hill, 428 pp.

Pfahl, S., P. A. O'Gorman, and M. S. Singh, 2015: Extratropical cyclones in idealized simulations of changed climates. *J. Clim.*, **28**, 9373–9392.

Pfahl, S., and M. Sprenger, 2016: On the relationship between extratropical cyclone precipitation and intensity. *Geophys. Res. Lett.*, **43**, 1752–1758.

Pinto, J. G., T. Spangehl, U. Ulbrich, and P. Speth, 2005: Sensitivities of a cyclone detection and tracking algorithm: individual tracks and climatology. *Meteor. Z.*, **14(6)**, 823-838.

——, ——, ——, ——, 2006: Assessment of winter cyclone activity in a transient ECHAM4-OPYC3 GHG experiment. *Meteor. Z.*, **15(3)**, 279-291.

——, U. Ulbrich, G. C. Leckebusch, T. Spangehl, M. Reyers, and S. Zacharias, 2007: Changes in storm track and cyclone activity in three SRES ensemble experiments with the ECHAM5/MPI-OM1 GCM. *Climate Dyn.*, **29**, 195–210.

Plante, M., S.-W. Son, E. Atallah, J. Gyakum,

and K. Grise, 2015: Extratropical cyclone climatology across eastern

Canada. *Int. J. Climatol.*, **35**, 2759–2776.

Pithan, F., T. G. Shepherd, G. Zappa, and I. Sandu, 2016: Climate model biases in jet streams, blocking and storm tracks resulting from missing orographic drag. *Geophys. Res. Lett.*, **43**, 7231–7240.

Raible, C. C., 2007: On the relation between extremes of midlatitude cyclones and the atmospheric circulation using ERA40. *Geophy. Res. Lett.*, **34 ,** L07703.

——, M. Messmer, F. Lehner, T. F. Stocker, and R. Blender, 2018: Extratropical cyclone statistics during the last millennium and the 21st century. *Climate Past*, **14**, 1499–1514.

Rantanen, M., J. Räisänen, V. A. Sinclair, and H. Järvinen, 2019: Sensitivity of idealised baroclinic waves to mean atmospheric temperature and meridional temperature gradient changes. *Climate Dyn.*, **52**, 2703–2719.

Sanders, F., and J. R. Gyakum, 1980: Synoptic–dynamic climatology of the "bomb." *Mon. Wea. Rev.,* **108,** 1589–1606.

Serreze, M. C., 1995: Climatological aspects of cyclone development and decay in the Arctic. *Atmos.–Ocean*, **33**, 1–23.

Seiler, C., 2019: A climatological assessment of intense extratropical cyclones from the potential vorticity perspective. *J. Climate*, **32**, 2369–2380.

——, and F. W. Zwiers, 2016: How well do CMIP5 climate models reproduce explosive cyclones in the extratropics of the Northern Hemisphere?. *Clim. Dyn.*, **46(3-4)**, 1241-1256.

——, ——, K. I. Hodges, and J. F. Scinocca, 2018: How does dynamical downscaling affect model biases and future projections of explosive extratropical cyclones along North America's Atlantic coast?. *Clim. Dyn*., **50(1)**, 677-692.

Screen, J. A. and I. Simmonds, 2013: Exploring links between Arctic amplification and mid-latitude weather. *Geophy. Res. Lett.*, **40**, 959–964.

Simpson, I. R., and Coauthors, 2020: An evaluation of the large-scale atmospheric circulation and its variability in CESM2 and other CMIP models. *J. Geophys. Res. Atmos.*, **125(13)**, e2020JD032 835.

Sinclair, M. R., 1994: An objective cyclone climatology for the Southern Hemisphere. *Mon. Wea. Rev.*, **122**, 2239–2256.

Son, H.-Y., J.-Y. Park, J.-S. Kug, J. Yoo, and C.-H. Kim, 2014: Winter precipitation variability over Korean Peninsula associated with ENSO. *Climate Dyn.*, **42**, 3171–3186.

Staten, P. W., K. M. Grise, S. M. Davis, K. Karnauskas, and N. Davis, 2019: Regional widening of tropical overturning: Forced change, natural variability, and recent trends. *J. Geophys. Res. Atmos.*, **124(12)**, 6104-6119.

Stoelinga, M. T., 1996: A potential vorticity-based study of the role of diabatic heating and friction in a numerically simulated baroclinic cyclone. *Mon. Wea. Rev.*, **124**, 849–874.

Taylor, K. E., R. J. Stouffer, and G. A. Meehl, 2012: An overview of CMIP5 and the experiment design. *Bull. Amer. Meteor. Soc.*, **93(4)**, 485-498.

Tierney, G., D. J. Posselt, and J. F. Booth, 2018: An examination of extratropical cyclone response to changes in baroclinicity and temperature in an idealized environment. *Clim. Dyn.*, **51(9–10)**, 3829–46.

Uccellini, L. W., and P. J. Kocin, 1987: The interaction of jet streak circulations during heavy snow events along the east coast of the United States. *Wea. Forecasting*, **2 ,** 289–308.

Ueda, H., Y. Amagai, and M. Hayasaki, 2017: South-coast cyclone in Japan

during El Nino-caused warm winters. *Asia-Pacific J. Atmos. Sci.*, **53(2)**, 287–293.

Ulbrich, U., J. G. Pinto, H. Kupfer, G. C. Leckebusch, T. Spangehl, and M. Reyers, 2008: Changing Northern Hemisphere storm tracks in an ensemble of IPCC climate change simulations. *J. Climate*, **21(8)**, 1669-1679.

Wang, B., R. Wu, and X. Fu, 2000: Pacific–East Asian teleconnection: How does ENSO affect East Asian climate? *J. Climate*, **13,** 1517–1536.

Wang, J., H.-M. Kim, E. K. M. Chang, 2017: Changes in northern hemisphere winter storm tracks under the background of Arctic amplification. *J. Clim.*, **30(10)**, 3705–24.

Wang, X., P. Zhai, and C. Wang, 2009: Variations in extratropical cyclone activity in northern East Asia. *Adv. Atmos. Sci.*, **26 ,** 471–479.

Wernli, H., S. Dirren, M. A. Liniger, and M. Zillig, 2002: Dynamical aspects of the life cycle of the winter storm Lothar (24–26 December 1999). *Quart. J. Roy. Meteor. Soc.*, **128 ,** 405–429.

——, and C. Schwierz, 2006: Surface cyclones in the ERA-40 dataset (1958–2001). Part I: Novel identification method and global climatology. *J. Atmos. Sci.*, **63**, 2486–2507.

Whittaker, L. M., and L. H. Horn, 1984: Northern Hemisphere extratropical cyclone activity for four mid-season months. *J. Climatol.,* **4,** 297–310.

Yamamoto, M., and N. Hirose, 2007: Impact of SST reanalyzed using OGCM on weather simulation: A case of a developing cyclone in the Japan-Sea area. *Geophys. Res. Lett.*, **34 ,** L05808.

Yang, M., X. Li, R. Zuo, X. Chen, and L. Wang, 2018: Climatology and interannual variability of winter North Pacific storm track in CMIP5 models. *Atmosphere*, **9**, 79.

Yoshida, A., and Y. Asuma, 2004: Structures and environment of explosively developing extratropical cyclones in the Northwestern Pacific region. *Mon. Wea. Rev.*, **132 ,** 1121–1142.

Zappa, G., L. C. Shaffrey, K. I. Hodges, P. G. Sansom, and D. B. Stephenson, 2013: A multimodel assessment of future projections of North Atlantic and European extratropical cyclones in the CMIP5 climate models. *J. Climate*, **26(16)**, 5846-5862.

——, M. K. Hawcroft, L. Shaffrey, E. Black, and D. J. Brayshaw, 2015: Extratropical cyclones and the projected decline of winter Mediterranean precipitation in the CMIP5 models. *Clim. Dyn.*, **45(7-8)**, 1727-1738.

Zhang, Y. X., Y. H. Ding, and Q. P. Li, 2012: A climatology of extratropical cyclones over East Asia during 1958–2011. *Acta Meteor. Sin.*, **26**, 261–277.

국문 초록

동아시아 온대저기압과 이들의 미래 온난 기후에서의 변화

이재연

지구환경과학부

서울대학교 대학원

동아시아 온대저기압은 강우나 황사와 같은 다양한 기상 현상을 동반하는 대표적인 중위도 시스템 중에 하나이다. 본 연구에서는 동아시아 온대저기압들의 기후학적인 특성을 이해하고 이들이 지구온난화에 따른 미래 기후에서 어떻게 변할지를 분석하였다. 이때 온대저기압은 850 hPa 등압면의 상대와도 장에서 탐지되었으며 자동화된 알고리즘을 이용하여 추적되었다.

먼저 ERA-Interim 재분석 자료를 이용하여 현재 동아시아 온대저기압의 특성을 살펴보았다. 동아시아 온대저기압은 알타이-사얀 산맥과 티베트 고원 풍하측에서 발달하는 대륙성 저기압과 경압성이 강한 쿠로시오-오야시오 발산대에서 발달하는 해양성 저기압으로 나뉠 수 있다. 이들 온대저기압들은 몽골과 쿠로시오 해류가 지나는 지역에서 가장 강한 활동성을 보이며 해수면 온도 경도가 매우 큰 쿠로시오-오야시오 발산대에서 가장 빠르게 발달한다. 특히 이들 온대저기압들 중에서 대륙성 저기압들은 경압성이 강한 겨울철이 아닌 봄철에 활동성이 가장 강한 독특한 계절성을 가진

다. 이러한 독특한 계절성을 가지는 대륙성 저기압들은 최근 약 40년간 그 수가 줄어드는 경향성을 보였다.

재분석 자료의 결과를 바탕으로 현재 동아시아 온대저기압의 기후학적인 특성들이 CMIP5 기후 모형에서 어느 정도 모의가 되는지, 미래 온난 기후 시나리오에서 어떻게 변하는지를 분석하였다. 이 때 분석에 사용한 CMIP5 기후 모형들은 산악 지형 위에서 결측 값을 제공하지 않는 9 개의 모형들로 구성하였다. 정성적으로 동아시아 온대저기압들의 기후학적인 특성은 CMIP5 기후 모형들에 의해서 잘 모의가 되었다. 하지만 산악 지형의 풍하측과 바다 위에서 정량적인 편차가 존재하는 것이 확인되었다. 이와 같은 편차들은 특히 낮은 격자 해상도와 산악 지형 해상도를 가지는 모형들에서 크게 나타났다.

기후 모형의 모사 능력은 미래 기후 시나리오의 결과에 영향을 줄 수 있기 때문에 9 개의 기후 모형들 중에서 가장 좋은 모사 능력을 가지는 5 개의 모형들을 이용하여 미래 동아시아 온대저기압의 변화를 살펴보았다. 동아시아 온대저기압들은 미래 온난 기후에서 빈도수가 줄어들고 강도가 약해지는 모습을 보였다. 이러한 CMIP5 기후 모형에서의 결과들은 최신 기후 모형인 CMIP6 모형들에서도 동일하게 확인이 되었다. 이러한 미래 동아시아 온대저기압들의 변화를 이해하기 위해서 미래 동아시아 지역의 경압성 변화를 살펴보았다. 그 결과 동아시아 온대저기압의 감소와 약화가 발생하는 지역의 부근에서 경압성이 국지적으로 약화되는 것이 확인되었다. 이러한 약화된 경압성은 미래 연직 바람 시어의 약화와 정적 안정도의 증가로 인한 것으로 확인되었다.

미래 경압성의 약화와 동아시아 온대저기압의 약화의 관계를

보다 자세히 살펴보기 위해서 이상 실험을 진행하였다. 이상 실험에서는 경압성에 영향을 줄 수 있는 요인인 연직 바람 시어와 정적 안정도를 조절하기 위해서 상층 동서 바람의 강도와 잠재 온도의 연직 기울기에 변화를 주었다. 실험을 통해서 배경장의 경압성이 약화될 때 온대저기압의 강도가 약해지는 것을 확인하였으며 이러한 결과를 통해서 CMIP 기후 모형들의 결과를 재확인할 수 있었다. 뿐만 아니라 실험을 통해서 배경장의 경압성이 매우 강해질 때에는 온대저기압의 강도가 경압성의 변화를 반드시 따르지는 않는다는 것을 추가적으로 확인할 수 있었다.

주요어: 온대저기압, 동아시아, 자동화된 저기압 추적 알고리즘, 지구 온난화, CMIP5, 이상 실험

학 번: 2018-37296